A Numerical Study of Stratified Airflow over Mesoscale Heat Sources with Application to Carolina Coastal Frontogenesis

LIAN XIE AND YUH-LANG LIN

Department of Marine, Earth and Atmospheric Sciences, North Carolina State University, Raleigh, North Carolina

(Manuscript received 8 March 1995, in final form 15 May 1996)

ABSTRACT

This paper presents the results from a numerical investigation of the responses of stratified airflow to prescribed near-surface mesoscale axisymmetric (circular) and elongated (elliptical) heat sources under uniform basic wind conditions using a simple three-dimensional model. Model results indicate that the structure of the response depends on the Froude number (Fr = V/NH) and the Rossby number (Ro = V/fL) associated with an axisymmetric thermal forcing, where H and L are the vertical and horizontal scales of the heat source, V the wind speed, N the Brunt–Väisälä frequency, and f the Coriolis parameter. However, the response to an elongated thermal forcing depends not only on the Froude and Rossby numbers, but also on the ratio of the alongstream scale (L_s) to the cross-stream scale (L_n) of the heat source, which are determined by the horizontal shape of the heat source and the direction of the basic flow. When L_s/L_n is less than 1, that is, the heat source is elongated in the cross-stream direction, the response resembles that of two-dimensional solutions. In this case, the heat-induced vertical motion is in phase with the heating field when Fr < 1 and is out of phase with the heating field when Fr > 1. Meanwhile, vertically propagating inertia–gravity waves are induced. However, when $L_s/L_n > 1$, that is, the heat source is elongated in the alongstream direction, the response appears quite different. In this case, the heat-induced vertical motion is primarily upward but confined to the lower atmosphere. The phase relationship between the vertical motion and the heating cannot be determined by the Froude number.

The horizontal distribution of surface sensible heat fluxes observed off the Carolina coast often appears to be elongated along the Gulf Stream front. These surface heat sources can induce coastal frontogenesis. In order to explain the effect of surface sensible heat fluxes on Carolina coastal frontogenesis, the shape factor of the heat source and the basic wind direction need to be taken into account.

1. Introduction

Understanding the formation of coastal fronts in the mid-Atlantic region is important for improving regional weather forecasts since coastal fronts in that region are often precursors of coastal cyclogenesis, which often brings heavy snow accumulations and strong winds along the east coast of the United States (Austin 1941; Bosart and Lin 1984; Uccellini et al. 1987). The general characteristics of coastal fronts have been extensively documented in the literature (Carson 1950; Ballentine 1980; Bosart 1975; Bosart and Lin 1984; Nielson 1989; Riordan 1990). Data collected during the Genesis of Atlantic Lows Experiment (GALE) indicate that coastal frontogenesis in the mid-Atlantic region is often associated with mesoscale surface confluence zones (SCZs) located offshore downwind of the Gulf Stream front (Riordan 1990). In fact, SCZs appeared in almost every coastal frontogenesis case during the GALE winter period of about 60 days (Riordan and

Lin 1992). Riordan (1990) pointed out that these SCZs as well as surface diffluence zones (SDZs) influence the evolution and westward progression of coastal fronts. For example, the flow is frontogenetic (frontolytic) within an SCZ (SDZ). In the case of the Carolina coastal front where the SDZ often lies to the east of the SCZ under northeasterly and easterly basic winds, a coastal front propagating from farther offshore may appear to jump from just east of the SDZ to the SCZ near the coast.

Riordan and Lin (1992) have shown that the confluence–diffluence flow pattern observed during GALE can be induced by diabatic heating. Using a linear theory with two prescribed elliptic heat sources, they were able to reproduce the observed confluence–diffluence flow pattern during coastal frontogenesis. They further suggested that the confluence–diffluence pattern may be related to the horizontal distribution of diabatic heating. The sensitivity of stratified airflow to the horizontal distribution of prescribed heating has been investigated by Hsu (1987) in a study of the heating-induced snowstorms in the vicinity of Lake Michigan. Hsu found that the orientation of basic wind to the heating pattern is crucial to the structure of the disturbances. The low-level heating associated with the relatively warm lake

Corresponding author address: Dr. Lian Xie, North Carolina State University, Box 8208, Raleigh, NC 27695-8208.
E-mail: xie@meavax.nrrc.ncsu.edu

surface produced three updraft bands under a westerly wind, two under a northwesterly wind, and one under a northerly wind.

In the studies cited above, the heat sources were assumed to be steady and therefore may be represented by a prescribed distribution function. In doing so, the mathematical problem reduces to a stably stratified flow over a prescribed thermal forcing. Such an approach was pioneered by Malkus and Stern (1953) in a study of the heat island problem. Their solution, which showed that the air ascends over the heat island, was later shown to be incorrect if a correct upper boundary condition is imposed (Olfe and Lee 1971; Smith and Lin 1982). Observations of airflow over heat islands showed a negative relationship between heating and vertical velocity; that is, there exists a region of descending motion over the heat island, followed by an ascending motion over the ocean on the downwind side during the daytime (Garstang et al. 1975; Mahrer and Pielke 1976). This negative (out of phase) relationship can be explained by linear theories of uniform stratified airflow over a two-dimensional (2D), near-surface mesoscale heat source (Lin and Smith 1986; Bretherton 1988). These theories suggest that for a nonrotating airflow the phase relationship between the heat source and the induced vertical motion depends on the Froude number associated with the thermal forcing, $Fr = V/NH$, where V is the wind speed, N the Brunt–Väisälä frequency, and H the vertical scale of the heat source. When the Froude number is much less than 1, the ascending motion occurs primarily over the heating region. As the Froude number increases, the center of the ascending motion shifts downstream, while a descending motion moves toward the heat source from upstream. A negative phase relationship is reached when the Froude number becomes greater than 1. This is often the case in the heat island problem, where heating is usually confined near the surface and thus the Froude number is almost always greater than 1.

Although linear theories on stratified flow responses to 2D mesoscale heat sources have been well established by now (e.g., Lin and Stewart 1991; Lin 1994a), the response to three-dimensional, mesoscale heat sources is far from complete. It is poorly understood how elongated heat sources similar to those frequently observed in the vicinity of the Gulf Stream front during winter may affect the airflow passing them. The linear theory of Riordan and Lin (1992) was quite successful in explaining the effects two isolated, elliptic heat sources at the surface may have on Carolina coastal frontogenesis. However, they did not examine the sensitivity of the response to the shape of the heat source, or the speed and direction of the basic wind. Furthermore, the applicability of their linear theory may be limited since the feedback between heating-induced wind speed and direction can be significant, in which case the response is fundamentally nonlinear even if the basic wind and the heat source are steady. This raises several important questions.

1) What are the differences between the airflow response produced by a 3D axisymmetric heat source as compared to a 3D elongated heat source?

2) What are the differences between the airflow response produced by a 2D heat source as compared to a 3D elongated heat source?

3) What are the differences between the linear and nonlinear responses to a 3D elongated heat source?

To address these questions, we will extend the linear theory developed by Riordan and Lin (1992) to a nonlinear dynamic framework using a hydrostatic, primitive equation model. We will compare the nonlinear responses to an elongated heat source with corresponding linear responses to the same heat source and with nonlinear responses to axisymmetric heat sources under similar dynamic regimes determined by the Froude number and Rossby number ($Ro = V/fL_s$). Here f is the Coriolis parameter, and L_s is the alongstream scale of the heat source. Following Riordan and Lin (1992), the heating field is prescribed. This type of approach has been shown to be useful in understanding the dynamics of a variety of thermally forced mesoscale circulations (e.g., see Lin and Stewart 1991 and Lin 1994a,b for reviews). Furthermore, by assuming a steady heat source, the feedback effect of surface winds on the heat source is excluded, so we can isolate nonlinear advective effects. The nonlinear coupling between the surface wind field and the diabatic heating will be addressed in a separate paper.

The rest of the text is organized as follows. In section 2, we briefly describe the numerical model used in this study and outline the experiment design. In section 3, we present the results from a set of nonlinear, numerical experiments with axisymmetric heat sources. Nonlinear responses to elongated heat sources are examined in section 4. The linear response to an elongated heat source is presented in section 5. A conceptual model based on the results from this study and its potential application to coastal fronto- and low-level jetogenesis off the Carolinas is discussed in section 6. Major conclusions are summarized in section 7.

2. Model description and experiment design

a. The governing equations

The model is based on the three-dimensional nonlinear primitive equations governing diabatically and orographically forced finite-amplitude perturbations in a continuously stratified, Boussinesq atmosphere in the terrain-following vertical coordinate $\sigma = (z - z_s)(z_t - z_s)^{-1}$, where $z_s(x, y)$ is the lower boundary and z_t is the top of the computational domain. In this study, the lower boundary is treated as a flat surface as in the case of a smooth sea surface. The σ coordinate has been retained for convenience. The governing equations are given by

$$\frac{\partial u}{\partial t} + (U + u)\frac{\partial u}{\partial x} + (V + v)\frac{\partial u}{\partial y} + \dot{\sigma}\left(\frac{\partial U}{\partial \sigma} + \frac{\partial u}{\partial \sigma}\right) - f_0 v + \frac{1}{\rho_0}\frac{\partial p}{\partial x} + g\left(\frac{z_t - \sigma}{z_t}\right)\frac{\partial z_s}{\partial x} + \nu u = 0 \qquad (1)$$

$$\frac{\partial v}{\partial t} + (U + u)\frac{\partial v}{\partial x} + (V + v)\frac{\partial v}{\partial y} + \dot{\sigma}\left(\frac{\partial V}{\partial \sigma} + \frac{\partial v}{\partial \sigma}\right) + f_0 u + \frac{1}{\rho_0}\frac{\partial p}{\partial y} + g\left(\frac{z_t - \sigma}{z_t}\right)\frac{\partial z_s}{\partial y} + \nu v = 0 \qquad (2)$$

$$\frac{1}{\rho_0}\frac{\partial p}{\partial \sigma} - \left(\frac{z_t - z_s}{z_t}\right)\frac{g}{\bar{\theta}}\theta = 0 \qquad (3)$$

$$\frac{\partial}{\partial x}[(z_t - z_s)u] + \frac{\partial}{\partial y}[(z_t - z_s)v] + \frac{\partial}{\partial \sigma}[(z_t - z_s)\dot{\sigma}] = 0 \qquad (4)$$

$$\frac{\partial \theta}{\partial t} + (U + u)\left(\frac{\partial \bar{\theta}}{\partial x} + \frac{\partial \theta}{\partial x}\right) + (V + v)\left(\frac{\partial \bar{\theta}}{\partial y} + \frac{\partial \theta}{\partial y}\right) + \dot{\sigma}\left(\frac{\partial \bar{\theta}}{\partial \sigma} + \frac{\partial \theta}{\partial \sigma}\right) + \nu\theta = \frac{\theta_0}{c_p T_0}Q, \qquad (5)$$

where

u	perturbation velocity in the x direction
v	perturbation velocity in the y direction
$\dot{\sigma}$	sigma vertical velocity (also denoted as w in the text)
p	pressure perturbation
θ	perturbation potential temperature
$U(\sigma)$	basic wind velocity in the x direction
$V(\sigma)$	basic wind velocity in the y direction
$\bar{\theta}(x, y, \sigma)$	basic-state potential temperature
$\nu(\sigma)$	coefficient of Rayleigh friction and Newtonian cooling
ρ_0	reference basic-state density (1.1614 kg m^{-3})
g	gravitational acceleration (9.80665 m s^{-2})
f_0	Coriolis parameter (7.943 × 10^{-5} s^{-1})
c_p	specific heat capacity of dry air at constant pressure (1004 J K^{-1} kg^{-1})
T_0	constant reference temperature (300 K)
θ_0	reference potential temperature (300 K)
N	Brunt–Väisälä frequency (0.01 s^{-1})
$Q(t, x, y, \sigma)$	diabatic forcing per unit mass.

In deriving (1)–(5), the hydrostatic equation has been used. The governing equations are discretized and numerically integrated over an unstaggered grid in (x, y, σ) space. The exact values of the horizontal (vertical) partial derivatives appearing in the momentum, continuity, and thermodynamic energy equations are approximated using a fourth-order (second order) centered finite-differencing scheme. The Eulerian local accelerations or temporal derivatives appearing in the zonal momentum, meridional momentum, and thermodynamic energy equations, which compose the three prognostic equations of the numerical model, are approximated through the leapfrog scheme, with the exception of the first time step, which is computed by forward finite differencing. A five-point numerical smoother is applied to suppress the spurious growth of high-wavenumber modes that may be introduced by various truncation errors of the numerical integration.

Within the σ-coordinate system, the lower boundary condition is simply that $\dot{\sigma} = 0$. In this study, the lower boundary is flat. Thus, the σ coordinate coincides with the z coordinate. The upper boundary condition is taken to be the radiation condition implemented through the numerical algorithm proposed by Klemp and Durran (1983). The lateral boundary conditions are specified through the zero-gradient constraint (e.g., Pielke 1984). The basic wind velocity (U, V) is assumed constant with height in this study. A 2D version of this model with subgrid mixing has been tested rigorously for flow over an isolated mountain ridge (Lin and Wang 1996). Details of the 3D model used in this study can be found in Weglarz (1994).

The horizontal grid intervals adopted in this study are $\Delta x = 5$ km and $\Delta y = 10$ km. The horizontal domain size is 320 (640) km in the x (y) direction. Sensitivity simulations with 21 levels and $\Delta z = 500$ m as well as 42 levels and $\Delta z = 250$ m have been conducted for the heating field described by (6), with no significant differences. Thus, only the low-vertical-resolution ($\Delta z = 500$ m and 21 levels) experiments will be described. The corresponding time step Δt for all experiments is 5 s.

The near-surface heating field is prescribed by the following function:

$$Q(x, y, z) = \frac{Q_0 h(z)}{[(x/a_x)^2 + (y/a_y)^2 + 1]^{3/2}}, \qquad (6)$$

where a_x and a_y are the half-width of the horizontal heating scale in the x and y directions, respectively, and $h(z)$ is the vertical distribution function. In this study, we have set

$$h(z) = \begin{cases} 1, & z \le 1 \text{ km} \\ 0, & z > 1 \text{ km} \end{cases} \qquad (7)$$

and $Q_0 = 0.2$ J kg^{-1} s^{-1}, which are typical parameters for a mesoscale heat source that represents surface sensible heat fluxes over the ocean off the Carolina coast

during winter (e.g., Riordan and Lin 1992). In this study, the atmosphere is assumed inviscid ($\nu = 0$), so the results can be compared with those of linear inviscid theories.

b. Experiment design

Ten experiments are carried out with prescribed heat sources whose horizontal and vertical structures are described, respectively by (6) and (7). The horizontal scale parameters, ambient wind speed and direction, and the linear-or-nonlinear option for each case are summarized in Table 1. All simulations are run for 24 h.

Cases 1–3 consider axisymmetric heat sources. The horizontal radius of the heat source is 35 km in cases 1 and 2, and is 15 km in case 3. An elliptical heat source is used in cases 4–10. The half-widths of the horizontal scales of the elliptical heat source in the x and y directions (short and long axes) for these experiments are $a_x = 15$ km and $a_y = 83$ km, respectively. Thus, the horizontal area of the elliptical heat source is about the same as that of the axisymmetric heat source used in cases 1 and 2, while a_x is identical to that in case 3. In all cases except cases 2 and 6, a 5 m s^{-1} basic wind speed, and thus a Froude number of 0.5, is assumed. The basic wind speed in cases 2 and 6 is assumed to be 15 m s^{-1}, which gives a Froude number of 1.5. The Rossby numbers in cases 1–10 are 0.89, 2.7, 2.08, 0.38, 2.08, 6.25, 0.74, 0.74, 0.38, and 2.08, respectively.

Cases 1–8 are nonlinear simulations, among which cases 1–3 are for axisymmetric heat sources and cases 4–8 are for the elliptical heat sources under different basic wind conditions. Cases 9 and 10 are corresponding linear simulations of cases 4 and 5. The separation of linear and nonlinear terms in the governing equations allows us to isolate the nonlinear effects. Thus, this study may be viewed as an extension of the linear theory of Riordan and Lin (1992).

3. Nonlinear responses to axisymmetric heating

In this section, we will present the results of three cases of nonlinear responses to axisymmetric heat sources with different Froude and Rossby numbers.

a. Surface structure

The 3D, nonlinear responses to mesoscale axisymmetric heat sources are considered in cases 1–3. Case 1 has a Rossby number of 0.89 and a Froude number of 0.5. The surface perturbation pressure, near-surface vertical velocity, and surface horizontal flow at 24 h for case 1 are shown in Figs. 1a–c, respectively. As illustrated in Fig. 1a, the surface pressure perturbation has two minima: one over the center of the heat source and the other located downstream. By examining the evolution of these two pressure minima from 6 (not shown) to 24 h, we find the one over the heat source is quasi-stationary, while the one located downstream is transient. Here, the word quasi-stationary means that there is no apparent displacement in the location of the first pressure minimum, which is located over the heat source, while "transient" refers to the gradual downstream expansion of the second pressure minimum, which has evolved into an elongated low pressure system by 24 h (Fig. 1a). The corresponding near-surface vertical velocity (which is actually at $z = 500$ m, the lowest model level above the surface) exhibits a phase shift between the centers of maximum ascending motion and maximum heating (Fig. 1b). The maximum of ascending motion (0.07 m s^{-1}) occurs approximately 25 km downstream of the heating center. Very weak descending motion (with a maximum speed of 0.01 m s^{-1}) can be seen farther downstream. Upstream of the heat source, there is only negligible descending motion (with a maximum speed of only 0.005 m s^{-1}). This is different from the response of airflow to 2D heat sources with a similar Froude number (e.g., Lin and Smith 1986) in which the airflow is known to descend just upstream of the 2D heat source. We will discuss this point in more detail in section 5. In the surface wind field (Fig. 1c), a SCZ occurs downstream of the heat source and a maximum wind speed zone (referred to as a low-level jet or LLJ hereafter) forms to the right of the confluence axis facing downstream. This LLJ is also elongated in the downstream direction similar to the second pressure minimum shown in Fig. 1a.

A comparison between the surface perturbation pressure and the perturbation winds (Fig. 1a) reveals that

TABLE 1. List of experiments.

Case	a_x (km)	a_y (km)	(U, V) (m s^{-1})	Type*	Fr	Ro
1	35	35	(0, −5)	NL	0.5	0.89
2	35	35	(0, −15)	NL	1.5	2.67
3	15	15	(0, −5)	NL	0.5	2.08
4	15	83	(0, −5)	NL	0.5	0.38
5	15	83	(−5, 0)	NL	0.5	2.08
6	15	83	(−15, 0)	NL	1.5	6.25
7	15	83	(−3.535, −3.535)	NL	0.5	0.72
8	15	83	(3.535, −3.535)	NL	0.5	0.72
9	15	83	(0, −5)	L	0.5	0.38
10	15	83	(−5, 0)	L	0.5	2.08

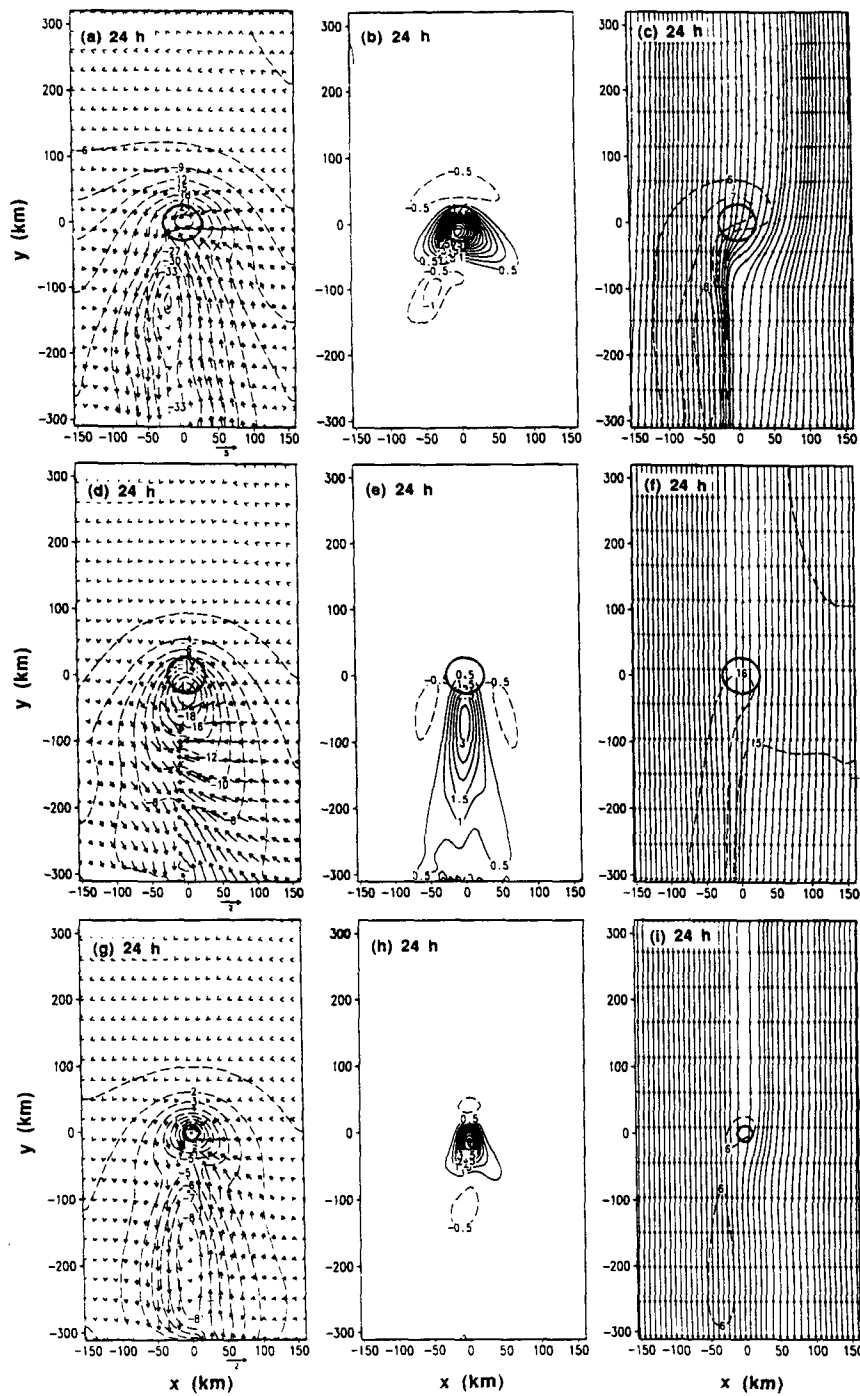* NL: nonlinear simulations; L: linear simulations.

FIG. 1. Surface perturbations induced by circular low-level heat sources at 24 h. (a) Surface pressure perturbation p' (Pa) and perturbation wind vectors (m s^{-1}) in case 1, (b) vertical velocity w (cm s^{-1}) at the lowest interior model level ($z = 500$ m) in case 1, and (c) streamline field and total wind speed contours for winds greater than the basic wind speed. The contours are drawn as broken lines at an interval of 1 m s^{-1}: (d)–(f) same as (a)–(c) but for case 2. (g)–(i) Same as (a)–(c) but for case 3. The 0.1 J kg^{-1} s^{-1} contour of Q_0 is highlighted by the thick solid circle centered at $(x, y) = (0, 0)$.

downstream of the heat source the perturbation wind vectors are nearly parallel to the isobars. This suggests that the earth's rotation measured by the Coriolis parameter f is important in case 1. This effect causes the asymmetry of the surface wind field induced by surface heating. For example, the wind speed is large to the right of the confluence axis facing downstream (Fig. 1c). Without rotation ($f = 0$), the induced surface wind field is symmetric about the confluence axis, which is located both over and downstream of the heat source (Xie and Lin 1994). The effect of rotation on the surface flow can be explained as follows. In the Northern Hemisphere, the Coriolis effect results in a rightward deflection. On the left side of the confluence axis facing downstream, this rightward deflection favors diabatically induced confluence, thus enhancing the deflection. On the right side of the confluence axis facing downstream, the diabatically induced deflection is leftward toward the confluence axis, which opposes the rightward deflection caused by the Coriolis effect, thus resulting in a weakened deflection. Similarly, winds to the right of the confluence axis tend to be stronger than those to the left because the direction of the perturbation winds is parallel (antiparallel) to the basic wind on the right (left) side of the confluence axis facing downstream.

Case 2 has a Rossby number of 2.7, which is greater than 1. Thus, the flow is expected to be ageostrophic. The Froude number in this case has a value of 1.5. The surface perturbation pressure at 24 h for case 2 is shown in Fig. 1d. A low pressure center with a minimum of 20 Pa is induced roughly 25 km downstream of the heating center. This pattern is obviously different from that in case 1 (Fig. 1a), where two different pressure minima can be identified: one over the heat source and the other downstream. The minimum perturbation pressure is much weaker than either pressure minimum in case 1. Although weak, the horizontal pressure gradient is considerably stronger on the upwind side of the low pressure center than on the downstream side. The perturbation winds with a maximum of only 2 m s^{-1} are also weaker than in case 1. The perturbation surface flow is mostly cross-isobaric, which is a strong indication that the response is primarily ageostrophic (Fig. 1d). The near-surface vertical velocity field is clearly out of phase with the heating field (Fig. 1e). Ascending motion occurs primarily downstream of the heat source. The maximum ascending motion is located roughly 75 km downstream of the heating center, with weak descending motion to the east and west of the ascending motion. Recall that in case 1 (Fig. 1b) the maximum ascending motion is shifted only about 25 km downstream of the heating center, but still occurs over the heat source, and a weak descending motion occurs farther downstream. This displacement of the ascending motion center downstream as the Froude number associated with the heating increases is consistent with 2D theories (Smith and Lin, 1982; Lin and Smith 1986; Raymond 1986). However, unlike the 2D

theories (as mentioned earlier), no significant descending motion occurs upstream of the heat source. In fact, descending motions induced by 3D axisymmetric heat sources are much weaker than the corresponding ascending motion and are located either downstream (case 1), or on each side (case 2), of the ascending motion. Figure 1f shows the streamline pattern of the total surface flow for case 2. As expected from the weaker perturbation flow seen in Fig. 1d, the streamlines are only weakly perturbed by the heat source. A weak SCZ can still be seen downstream of the heat source. The maximum wind speed is located to the left of the confluence zone facing downstream but is only about 1 m s^{-1} above the basic flow speed.

Case 3 has a moderate Froude number of 0.5 and a large Rossby number of 2.08. The surface perturbation pressure at 24 h for case 3 is shown in Fig. 1g. The general pattern is similar to that seen in Fig. 1a for case 1; that is, two separate pressure minima can be identified: one over the heat source and another farther downstream. However, the perturbation pressure is much weaker for this case, with a minimum of only 8 Pa. The perturbation flow is cross-isobaric near the heat source, indicative of an ageostrophic response there (Fig. 1g). The perturbation wind vectors are more parallel to the isobars associated with the downstream low pressure center, which is elongated in the alongstream direction. Thus, although the Rossby number associated with the heating is larger than 1, the flow downstream of the heat source may still be quasigeostrophic due to the growth of the alongstream scale of the perturbation pressure system. The near-surface vertical motion at 24 h for case 3 is shown in Fig. 1h. The general pattern is also similar to that seen in case 1 (Fig. 1b); that is, the center of ascending motion is shifted some 25 km downstream but still occurs over the heat source. The maximum ascending motion at this level is about 0.05 m s^{-1}, slightly weaker than that in case 1. Again, no significant descending motion can be identified. The streamline pattern of the total surface flow at 24 h for case 3 is shown in Fig. 1i. It is evident that only a weak SCZ is induced downstream of the heat source, similar to case 2 (Fig. 1f). The maximum wind speed is located to the right of the confluence zone facing downstream and is about 6 m s^{-1}, which is only 1 m s^{-1} above the basic wind speed. The fact that both cases 2 and 3 have a large Rossby number and weak response suggests that the intensity of surface response decreases as the Rossby number increases. On the other hand, the fact that both cases 1 and 3 have the same Froude number and similar phase relationships between the induced perturbations and the prescribed heating suggests that the horizontal pattern of the response is largely determined by the Froude number, at least as far as axisymmetric heat sources are concerned.

b. Vertical structure

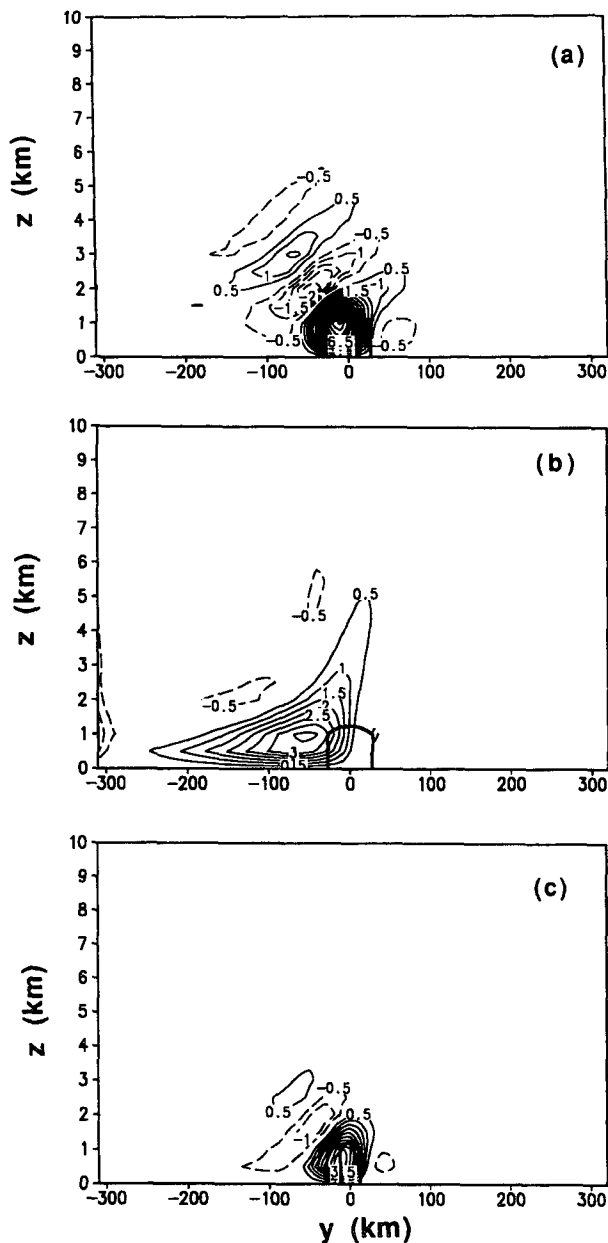We will now examine the vertical structure of the responses to 3D axisymmetric heat sources. Figure 2a

FIG. 2. Alongstream $(y-z)$ sections of vertical velocity (cm s^{-1}) across the heating center $(x, y) = (0, 0)$ at 24 h. (a)–(c) cases 1–3, respectively. The 0.1 J kg^{-1} s^{-1} contour of Q_0 is highlighted by the thick solid line.

shows the vertical velocity cross section at $x = 0$ km at 24 h for case 1. An inertia–gravity wave–like structure is generated, but it is primarily confined below a height of about 4 km. The maximum ascending motion occurs near the top of the heat source (~ 1 km) and has a value of about 0.09 m s^{-1}. The vertical velocity cross section at $x = 0$ km at 24 h for case 2 is shown in Fig. 2b. It is dominated by a localized region of ascending motion downstream of the heat source. It is similar to case 1 in that the heat-induced perturbation occurs pri-

marily in the lower atmosphere. However, the ascending motion for this case, which has a maximum of 0.035 m s^{-1} located near the top of the heat source (~ 1 km), extends to about 5 km over the heat source. The top of the ascending motion decreases as the airflow moves downstream. The vertical velocity cross section for case 3 along $x = 0$ km at 24 h is shown in Fig. 2c. Similar to cases 1 and 2, the heat-induced perturbation occurs primarily in the lower atmosphere. The maximum ascending motion (~ 0.05 m s^{-1}) is located near the 500-m level.

An intercomparison among the vertical structures for cases 1–3 indicates that

1) for an axisymmetric heat source, the heat-induced vertical motion occurs primarily in the lower atmosphere with a maximum near or below the top of the heat source; and

2) ascending motion extends to a higher elevation for larger–Froude number flow (case 2) than for smaller–Froude number flow (cases 1 and 3), since for a heat source of same depth, the vertical wavelength of the induced perturbation is directly proportional to the Froude number.

4. Nonlinear responses to elliptical heating

The responses of a stratified airflow to several 3D axisymmetric mesoscale heat sources presented in section 3 indicate that the effect of a 3D heat source may differ significantly from that of a 2D heat source. Observations made during the GALE field program off the Carolinas show that low-level heating over coastal waters often appears as isolated centers that are generally elongated with a major axis parallel to the oceanic front (Riordan 1990). The structure of these elongated heat sources lies between that of a 2D heat source parallel to the oceanic front and a 3D axisymmetric heat source, since a 2D heat source may be viewed as the limiting case of an elongated heat source with a large horizontal aspect ratio and an axisymmetric heat source may be seen as a special case of elongated heat source when its horizontal aspect ratio is 1. The latter may be considered as an approximate representation of the heating associated with an axisymmetric warm-core oceanic eddy. For an elongated heat source, the effective heating scale an airstream experiences depends on the angle between the airstream and the major axis of the heat source. This has some interesting consequences, as we will show below.

a. Responses under along-heating and cross-heating basic wind conditions

For an elongated heat source, we will refer to a basic flow that is parallel to the major axis of the heat source as an along-heating flow and, likewise, a basic flow that is normal to the major axis of the heat source as a cross-heating flow. In the cases to be presented below, the prescribed heat source is elliptical with the major axis

along the north–south direction. Thus, a northerly basic flow is an along-heating flow and an easterly basic flow is a cross-heating flow. The difference between these two cases will be examined below.

1) HORIZONTAL STRUCTURE

First, we consider a northerly basic wind parallel to the major axis of the heat source (case 4). The Froude number is 0.5, which is identical to that used in cases 1 and 3. The Rossby number is 0.38. Therefore, the induced flow should fall within the quasigeostrophic flow regime. In the following, we will show the simulated results at 24 h as well as at 12 h. The 24-h results can be compared with those shown in the last section for axisymmetric heat sources. The 12-h results are presented for the purpose of showing the time evolution in the horizontal structure of the heat-induced perturbations from 12 to 24 h. The time evolution of minimum pressure, maximum vertical velocity at $z = 500$ m, and maximum surface wind speed at 3-h intervals will be discussed later.

At 12 h, a negative surface pressure perturbation is induced downstream of the heat source (Fig. 3a). This low pressure center becomes more elongated and is advected downstream by 24 h (Fig. 3b). Notice that only one pressure minimum is induced, while for the circular heat source cases with the same Froude number (cases 1 and 3), two separate pressure minima can be identified (Figs. 1a and 1g). Downstream of the heat source, the perturbation wind vectors are closely aligned with the isobars, which is an indication of quasigeostrophic response in this region. However, upstream, near the heating center, the flow is primarily ageostrophic. The near-surface maximum ascending motion remains near the heating center throughout the 24-h simulation (Figs. 3c and 3d). Note that there is almost no phase shift between the vertical motion and the heating center, even though the Froude number is identical to that for cases 1 and 3. The surface wind field shows the existence of an SCZ along the western edge and downstream of the heat source at 12 h (Fig. 3e). The flow is asymmetric about the confluence axis with a maximum wind speed of about 8 m s^{-1}, which is located to the west of the heat source. The formation and the location of this wind speed maximum (the LLJ west of the heating) relative to the confluence axis partially support the conceptual model of Doyle and Warner (1993, their Fig. 23). This asymmetry in the flow field intensifies with time as reflected by the strengthening surface winds to the west and downstream of the heat source and by the westward deflection of winds on the east side of the confluence axis (Fig. 3f). The SCZ is roughly collocated with the surface pressure minimum (Figs. 3a and 3b), which is located downstream of the heat source.

The surface pressure perturbation, near-surface vertical velocity, and surface winds for case 5 (easterly basic wind) are shown in Fig. 4. Two pressure minima

can be identified at 12 h (Fig. 4a): one is located over the heat source, while the other is located farther downstream. Both pressure minima deepen with time but appear to be stationary from 12 to 24 h. The vertical velocity field at 500 m shows that descending motion occurs over the upstream portion of the heat source and that ascending motion occurs downstream (Figs. 4c and 4d). The zero vertical velocity contour passes through the center of the heat source. This suggests a 90° phase shift between the vertical velocity and the surface heating. This pattern remains quasi-stationary from 12 to 24 h. Surface wind speeds strengthen in the vicinity of the heat source at 12 h (Fig. 4e) and later extend to the north and east (upstream) of the heat source at 24 h (Fig. 4f).

A comparison between cases 4 and 5 reveals that for a moderate Froude number of 0.5 the following can be observed.

(i) A single, elongated pressure minimum is induced (downstream of the heat source) in the northerly (along-heating) basic wind condition ($L_s/L_n > 1$) (case 4), while two pressure minima (one over and the other downstream of the heat source) are induced in the easterly (cross-heating) basic wind condition ($L_s/L_n < 1$) (case 5).

(ii) In the along-heating basic wind condition ($L_s/L_n > 1$) (case 4), the vertical motion is in phase with the heating, that is, ascending motion is centered over the heat source. In the cross-heating basic wind condition ($L_s/L_n < 1$) (case 5), descending motion occupies roughly half the heating area, and the ascending motion is shifted farther downstream with a phase difference of approximately 90° from the heating center.

(iii) In both the along-heating and cross-heating cases, an SCZ is produced, as in the case of an axisymmetric heat source: in the former case ($L_s/L_n > 1$) (case 4), the SCZ extends from the western edge (to the right, facing downstream) of the heat source to an elongated area far downstream, while in the latter case ($L_s/L_n < 1$) (case 5), the SCZ occurs downstream of the heat source at a position about 50 km to the north (to the right, facing downstream) of the heating center.

(iv) Large winds occur primarily downstream and to the west (to the right, facing downstream) of the heating center under an along-heating basic wind condition ($L_s/L_n > 1$) (case 4) but over the heat source in the cross-heating basic wind condition ($L_s/L_n < 1$) (case 5).

Note that there is a significant difference in the phase relationship between the vertical motion and the heat source between cases 4 and 5. Although both cases have the same Froude number of 0.5, only in the latter case (case 5, easterly basic wind) does the vertical velocity show a significant phase shift from that of the heating as predicted by 2D linear theories for moderate–Froude number flow (e.g., Lin and Smith 1986). Recall that in case 2, a large Froude number (1.5) is used, but no significant descending motion occurs over
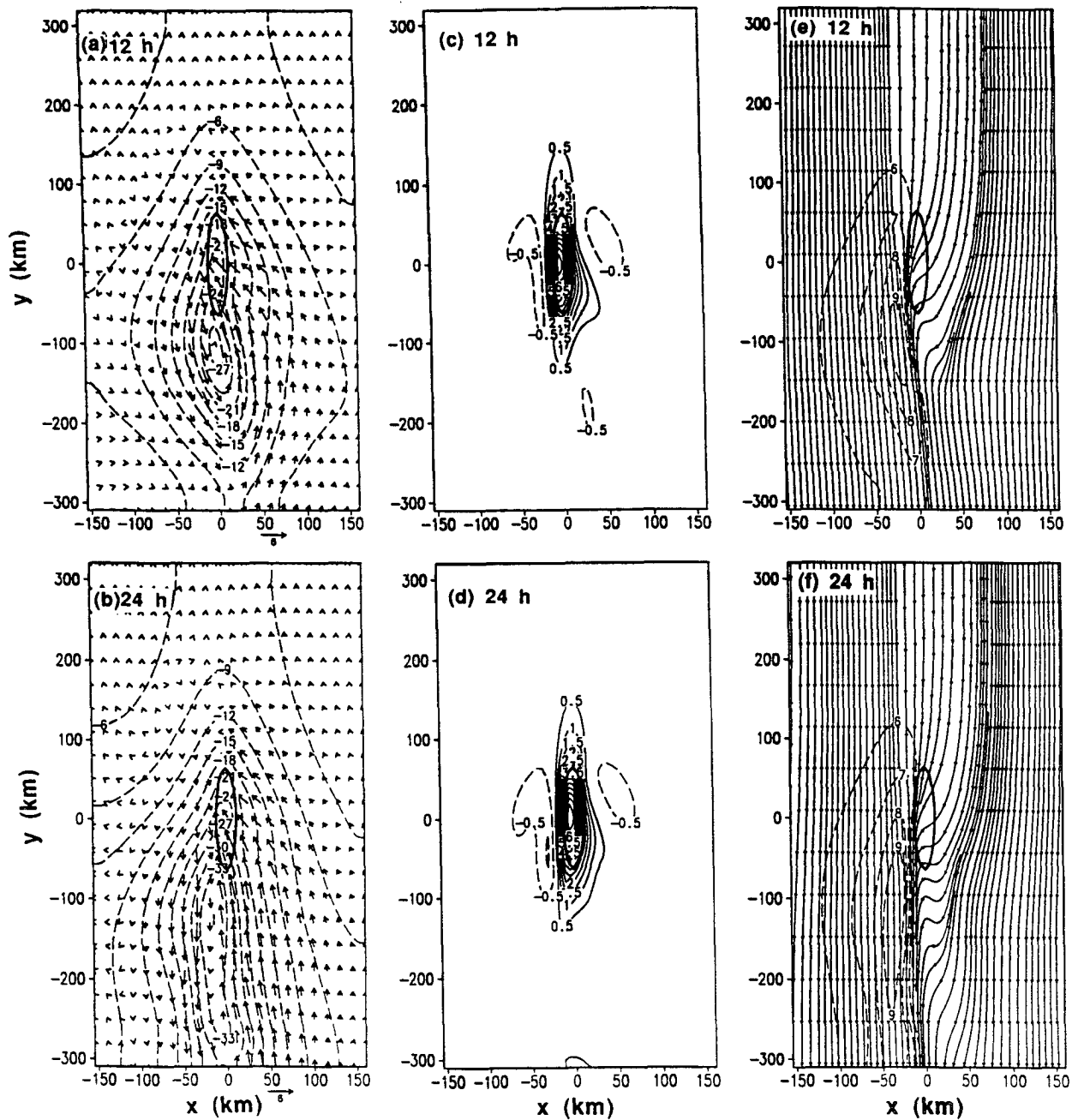
FIG. 3. Surface responses under northerly basic wind at 12 and 24 h for case 4. (a) Surface pressure (broken contours) and wind (vectors) perturbations at 12 h; (b) same as (a) but for 24 h. (c) Vertical velocity (cm s^{-1}) at the lowest level above the ground ($z = 500$ m) at 12 h; (d) same as (c) but for 24 h; (e) surface streamlines field at 12 h; contours of total wind speed greater than the basic wind speed are drawn as broken lines; (f) same as (e) but for 24 h. The 0.1 J kg^{-1} s^{-1} contour of Q_0 is highlighted by the thick solid oval centered at $(x, y) = (0, 0)$.

the heat source (Fig. 1e) although the ascending motion is completely out of phase with the heating maximum. Thus, an important question is whether a large–Froude number flow will exhibit such a phase difference if forced by an elongated mesoscale heat source. This is examined in case 6, which is the same as case 5 except that the basic wind speed is increased to 15

m s^{-1}, so the Froude number is 1.5, the same as in case 2.

Figures 5a and 5b show the surface pressure perturbation and perturbation winds at 12 and 24 h for case 6. They are almost the same, suggesting that a quasi-steady state has been reached. Only one low pressure center, which is located roughly 25 km downstream of
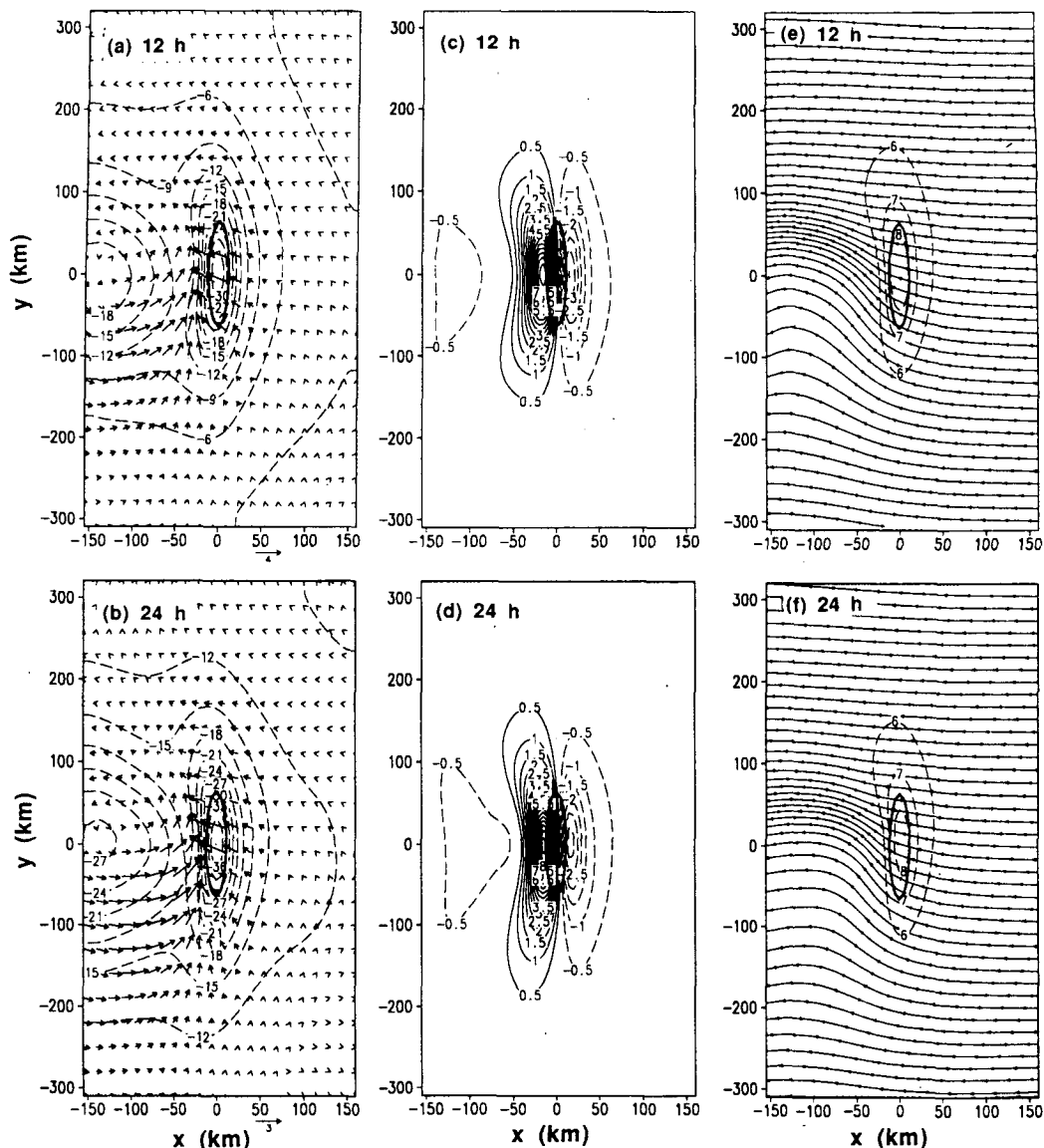
FIG. 4. Same as in Fig. 3 but for case 5.

the heating center, exists, while in case 5 the primary pressure minimum is collocated with the heating center (Figs. 4a and 4b). The pressure center in case 6 (with a minimum of −14 Pa at 24 h) is much weaker than that in case 5 (with a minimum of −37 Pa at 24 h). The near-surface vertical velocity fields at 12 and 24 h for case 6 are shown in Figs. 5c and 5d, respectively. No major changes occur from 12 to 24 h. A completely out-of-phase relationship exists between the vertical velocity and the heating, which is consistent with that predicted by 2D linear theories; that is, descending motion occurs over the heat source and ascending motion occurs downstream. Similar to the pressure perturbation, the vertical velocity is much weaker in case 6 than that in case 5. No significant wind acceleration occurs

in case 6, as indicated in the perturbation wind field (Figs. 5a and 5b) and in the total wind field (Figs. 5e and 5f).

2) VERTICAL STRUCTURE

The differences between along-heating and cross-heating basic wind cases show not only in the horizontal response patterns as presented above, but also in the vertical structure as we show below. To illustrate these differences, vertical velocity cross sections along the basic wind direction through the center of the heat source at 24 h will be examined.

The vertical velocity field at 24 h on the vertical cross section at $x = 0$ km for case 4 (northerly basic
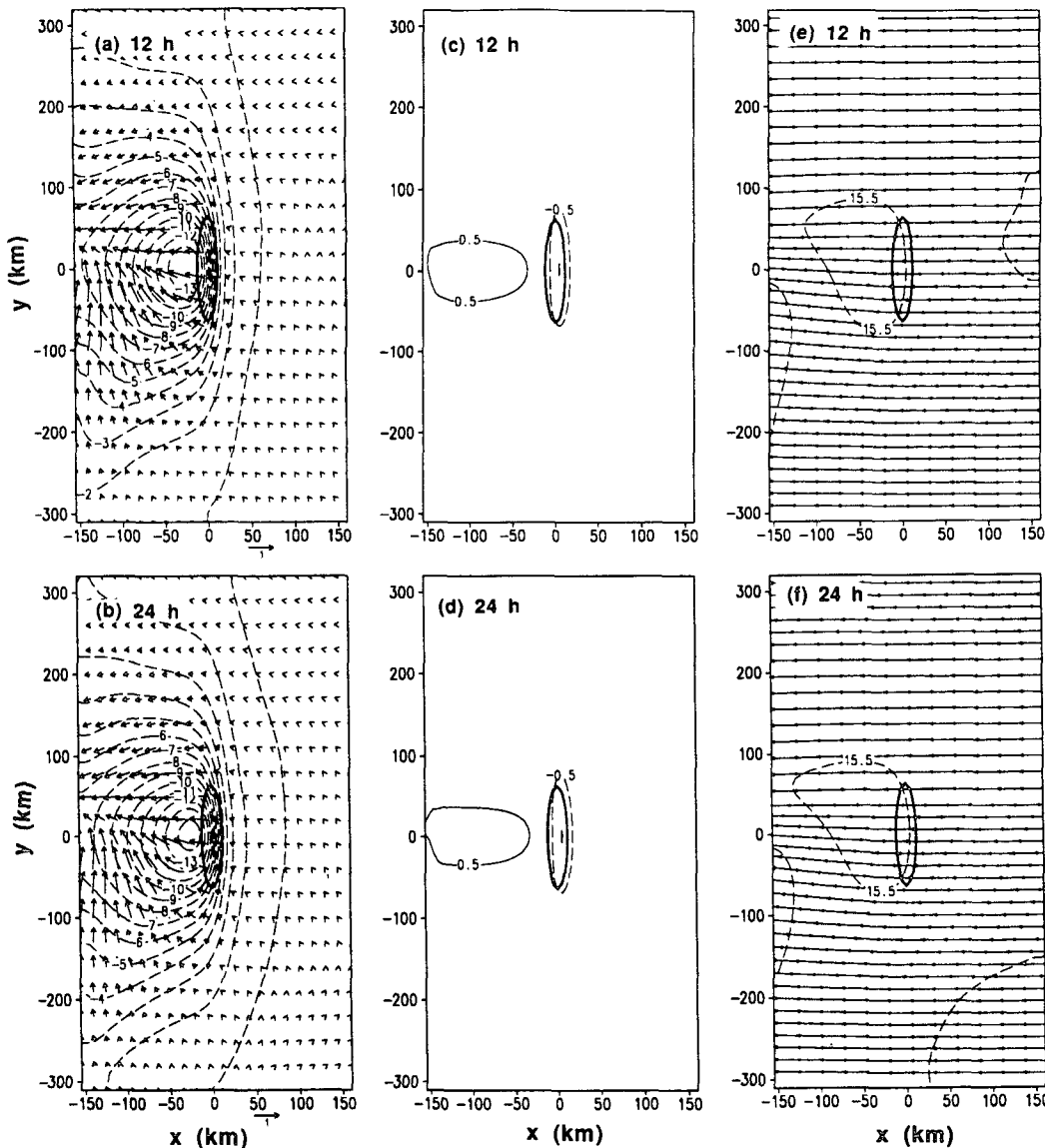
FIG. 5. Same as in Fig. 3 but for case 6.

wind) is shown in Fig. 6a. Upward motion is induced over the heat source, which is confined below 2 km. A region of weak ascending motion can be identified 200 km downstream of the heating center, suggesting downstream advection of the disturbance. No significant descending motion can be seen in this case. The disturbance in vertical motion for case 5 (easterly basic wind) is fundamentally different from that of case 4. Figure 6b shows the vertical velocity field at 24 h on a cross section at $y = 0$ km for case 5. The maximum ascending motion occurs near $z = 1$ km, just downstream of the heat source, while a low-level maximum in descending motion occurs upstream. The flow response is clearly a vertically propagating inertia–gravity wave. The vertically propagating wave train tilts

slightly downstream with height, which is caused by the effects of rotation. The vertical wavelength is approximately 3 km (Fig. 6b), which is consistent with that predicted by linear gravity wave theory (e.g., Smith 1979); that is, $2\pi V/N \sim 3.14$ km, where $N = 0.01$ s^{-1} is the Brunt–Väisälä frequency used in this study. Linear gravity wave theory also provides a reasonable estimate of the vertical wavelength for case 6 (Fig. 6c). The vertical wavelength predicted by linear theory is $2\pi V/N \sim 9.4$ km, which is approximately the same as the simulated vertical wavelength, that is, the distance between the two centers of descending motion, one at 1 km and the other slightly above 10 km, shown in Fig. 6c. The major differences between cases 5 and 6 are the following. 1) The vertical velocity is more
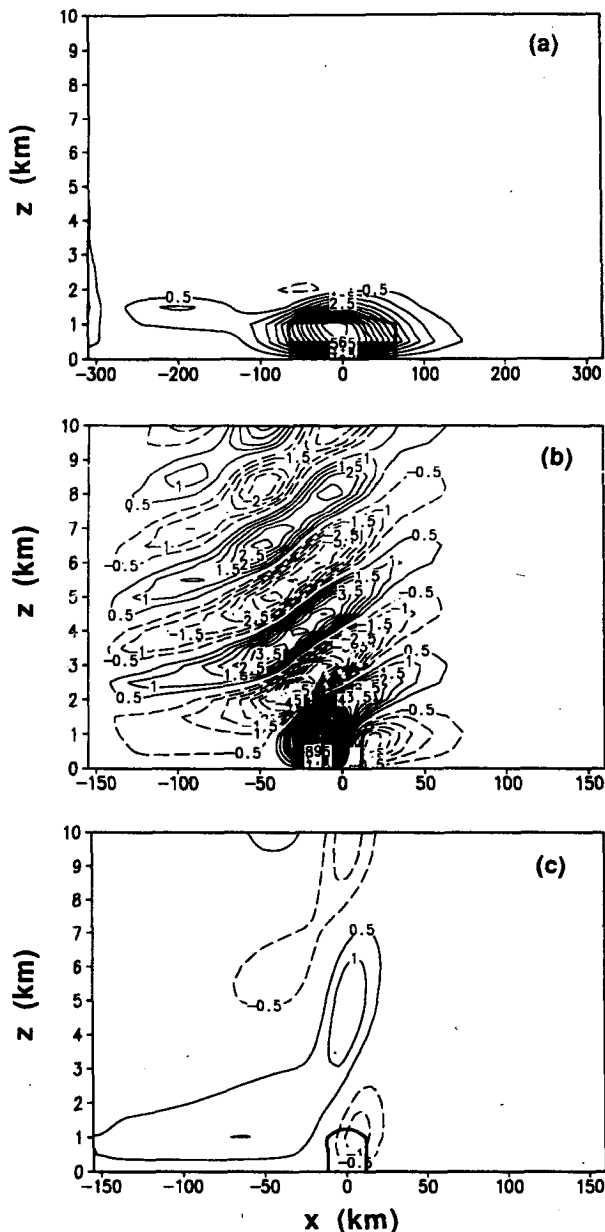
FIG. 6. Alongstream cross sections of vertical velocity across the center of the heat source $(x, y) = (0, 0)$ at 24 h. (a) Vertical cross section along $x = 0$ showing the vertical velocity under northerly basic wind (case 4). (b) Vertical cross sections along $y = 0$ km showing the vertical velocity under easterly basic wind (case 5). (c) Same as (b) but for case 6. The thick solid curve highlights the $Q_0 = 0.1$ J kg^{-1} s^{-1} contour of the heat source.

out of phase with the heating in case 6 than in case 5. Below $z = 1$ km, ascending motion occurs only downstream of the heat source, and descending motion occurs over the heat source (similar to that predicted by linear theories for large–Froude number airflow over a 2D heat source). 2) For case 6, the heating-induced disturbance propagates upward with negligible downstream tilting, because of the large Rossby number. 3)

The amplitude of the disturbance in the vertical motion field is much weaker in case 6 than in case 5.

The fact that vertically propagating disturbances are induced by heating in cases 5 and 6 but not in case 4 suggests that the direction of basic wind has a significant effect on the induced mesoscale circulation. This may be due either to the difference of the alongstream length scale of the heat source under different basic wind conditions, or to the ratio of the alongstream and cross-stream heating scales, which is determined by the horizontal aspect ratio of the heat source (a_x/a_y) and the basic wind direction. If the former is true, then we would have seen a vertically propagating wave in case 3 in which the alongstream heating scale is identical to those of cases 5 and 6. Thus, it is the aspect ratio, or more exactly, the two-dimensionality, of the elongated heat source in cases 5 and 6 that is responsible for the different flow responses. The model results suggest that when the basic wind is parallel to the major axis of an elongated heat source, the vertical velocity is confined to the lower atmosphere since the air parcels are able to go around the heat source (case 4, Fig. 6a), similar to three-dimensional mountain waves (e.g., Smith 1979), and when the basic wind is parallel to the short axis of an elongated heat source, vertically propagating inertia–gravity waves are produced (cases 5 and 6, Figs. 6b and 6c).

b. Basic winds with a 45° angle to the major axis of the heat source

In addition to the northerly and easterly basic winds, we have also examined the flow responses under northeasterly and northwesterly basic wind conditions. These two cases are of interest because of their relevance to synoptic conditions associated with cold-air outbreaks off the Carolinas.

Consider first a northeasterly basic wind that blows at a 45° angle to the major axis of the heat source (case 7). At 12 h two separate pressure perturbation centers can be seen: one over the heat source and the other downstream of the heat source (Fig. 7a), similar to case 5 (Fig. 4a). The former remains over the heat source from 12 to 24 h, and the latter drifts slowly downstream (Fig. 7b). Both pressure minima deepen with time. The vertical velocity at 12 h shows descending motion just upstream of the heating center followed by ascending motion over and downstream of the heat source (Fig. 7c). Notice that the maximum ascending motion is displaced downstream near the 0.1 J kg^{-1} s^{-1} contour line, similar to that in case 5. This pattern remains almost time independent from 12 to 24 h (Fig. 7d). The surface winds strengthen as the airstream approaches and crosses the heat source (Figs. 7e and 7f). Case 7 is also similar to case 5 in that both have a wind speed maximum over the heat source, which is almost constant from 12 to 24 h. Winds upstream and over the heat source increase substantially and reach a maximum value of 7.75 m s^{-1}. Similar to the pressure per-
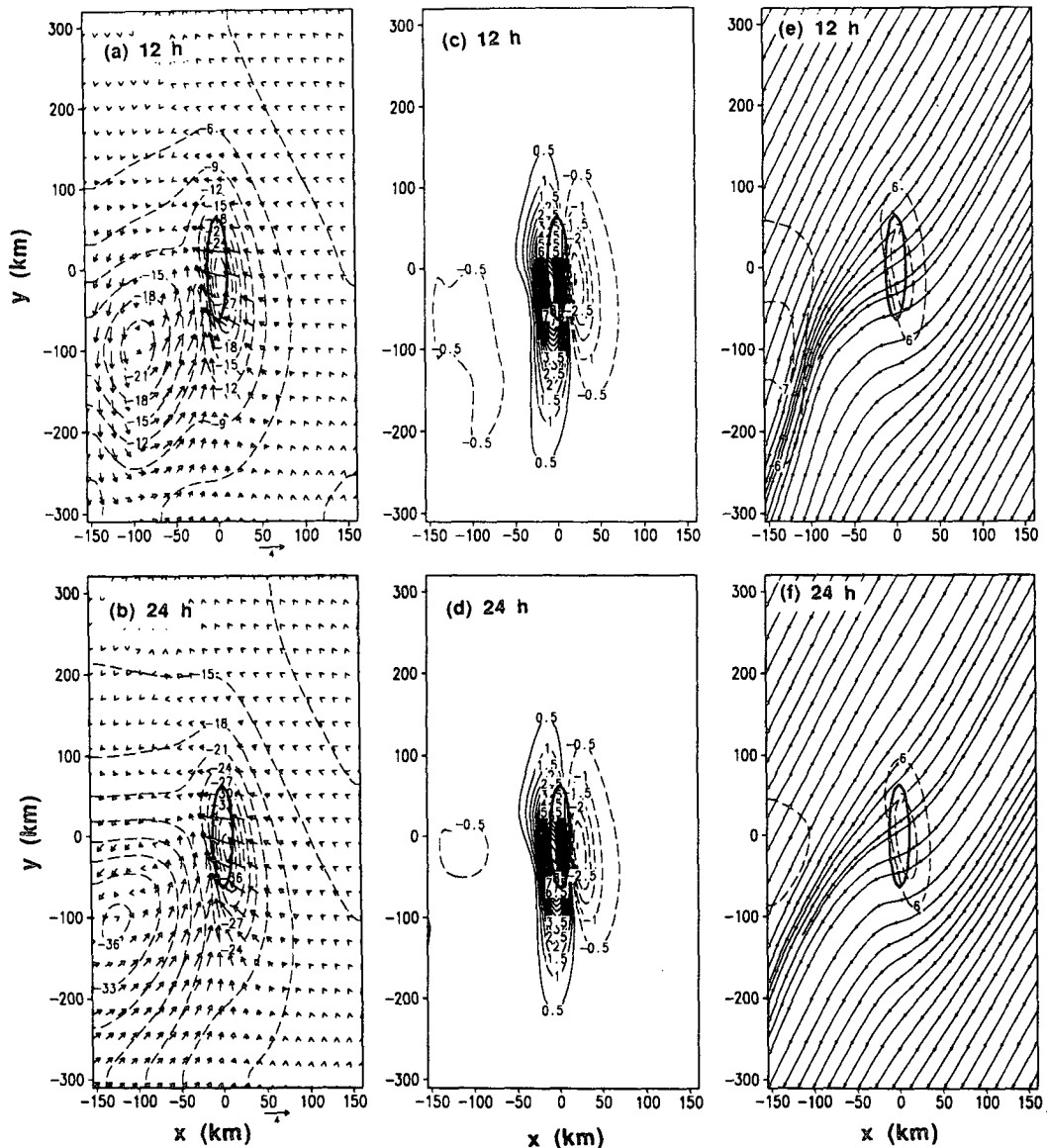
FIG. 7. Diabatically induced surface perturbations under a northeasterly basic wind (case 7) at 12 and 24 h.
Panels (a)–(f) correspond to Figs. 3a–f, respectively, except for case 7.

turbation, a second wind speed maximum can be seen downstream of the heat source. It appears that there exist two modes of heating-induced disturbances: a stationary mode, which remains in the vicinity of the heat source, and a transient mode, which propagates downstream from the heat source. Confluence occurs primarily downstream of the heat source throughout the 24-h simulation, which is consistent with observations (e.g., Riordan 1990).

We now consider a northwesterly basic wind (case 8) that represents a cold-air outbreak condition off the Carolinas. The 12- and 24-h responses of surface pressure, near-surface vertical velocity, and surface winds are shown in Fig. 8. The general patterns of surface

pressure, vertical motion, and surface wind fields may be viewed as the mirror images of the northeasterly basic wind case (Fig. 7). For example, at 12 h, the pressure perturbation (Fig. 8a) and the confluence zone (Fig. 8e) are located to the southeast of the heat source. The maximum ascending motion occurs just southeast of the heating center, with descending motion just west of the 0.1 J kg^{-1} s^{-1} heating contour (Fig. 8c). The responses at 24 h (Figs. 8b, 8d, and 8f) are generally similar to those at 12 h. However, some differences exist between case 8 and the mirror image of case 7 because of the Coriolis effect. For example, at 24 h, the flow over the heat source in case 8 (Fig. 8f) has a stronger southerly component than that in case 7 (Fig. 7f).
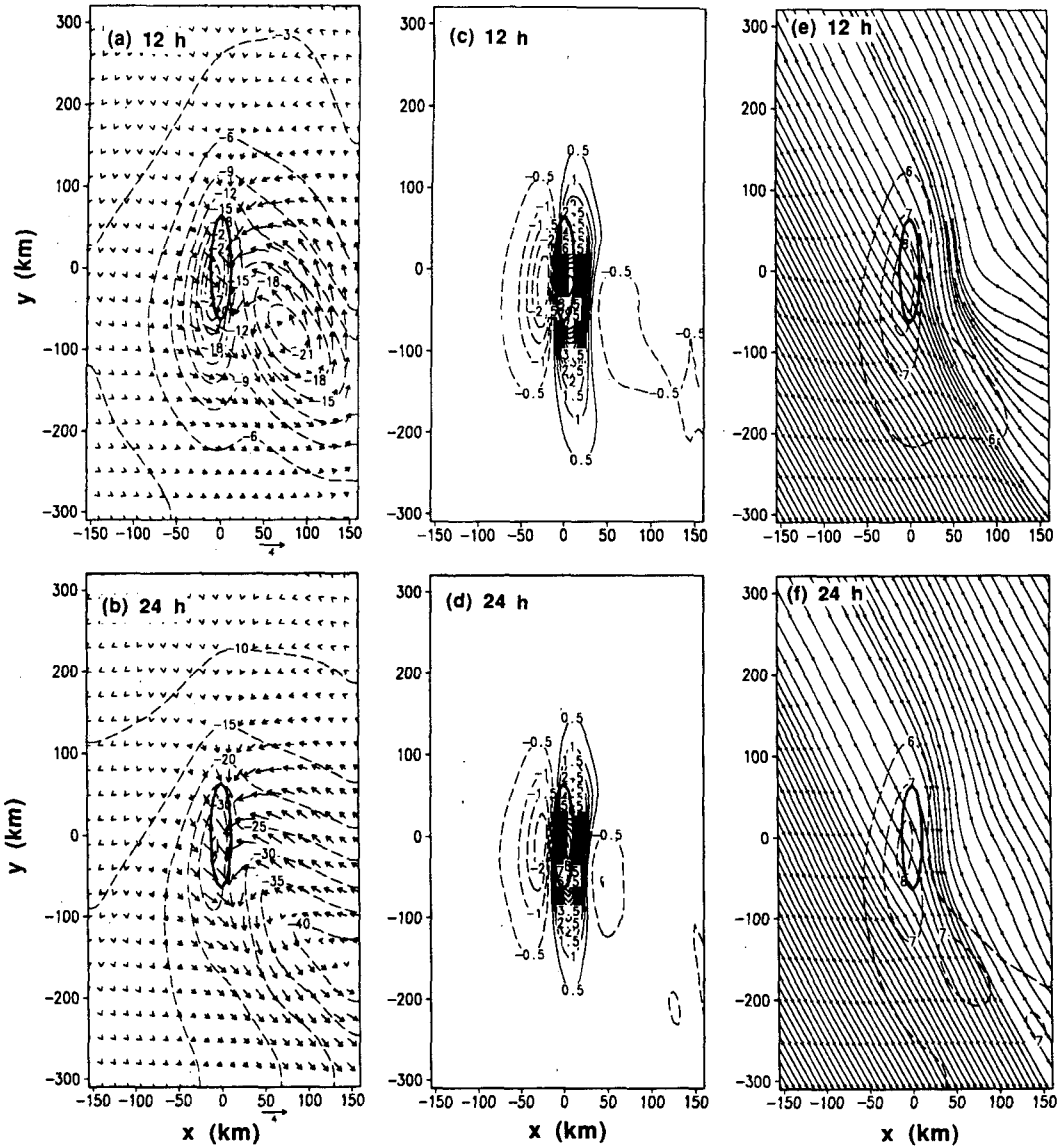
FIG. 8. Same as in Fig. 7 but for northwesterly basic wind (case 8).

c. Time evolution

To illustrate how the surface responses differ in the elongated heating cases under different basic wind conditions, we compare the time evolution of surface minimum pressure, maximum near-surface ascending motion, and maximum wind speed under northerly (case 4), easterly (case 5), and northeasterly (case 7) winds. As shown in Fig. 9, the vertical velocity increases steadily with time in cases 5 and 7 but decreases after 3 h in case 4. This results in a weaker vertical velocity in case 4 than in cases 5 and 7. On the other hand, although the final (24 h) minimum surface pressure in case 4 is slightly weaker than those in cases 5 and 7, the final maximum surface wind speed is the largest in case 4. These characteristics suggest that case 4 is more

geostrophic in nature than cases 5 and 7, as expected from the smaller–Rossby number flow that characterizes case 4.

5. Linear responses to elliptical heating

Before proceeding to the discussion of the significance of the results presented above, we will now compare them with the corresponding linear solutions. For convenience, our discussion will focus on northerly and easterly basic winds in which the basic wind is either parallel or normal to the major axis of the heat source. Such a comparison may provide us with clues on the importance of nonlinearity in the 3D response of stratified flow to a prescribed mesoscale heat source.
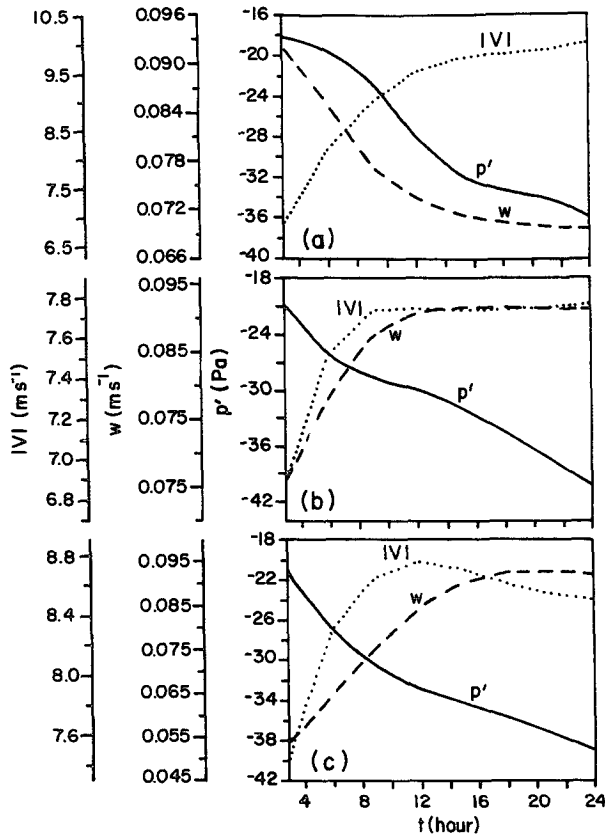
FIG. 9. Time evolutions of extrema of surface perturbations induced by diabatic heating. Simulation time (h) is labeled along the horizontal axis. Solid curve: surface pressure minimum (Pa); broken curve: maximum vertical velocity at $z = 500$ m (m s^{-1}); dotted curve: maximum surface wind speed (m s^{-1}). (a) Northerly basic wind (case 4), (b) northeasterly basic wind (case 7), and (c) easterly basic wind (case 5).

Consider first the northerly basic wind case (case 9). The patterns of surface wind, perturbation pressure, and near-surface vertical velocity are found to be similar to the corresponding nonlinear case (case 4), but the intensity of the response in the linear case differs somewhat from that in the nonlinear case. To illustrate this, we have presented in Fig. 10 the surface perturbation pressure, near-surface vertical velocity, and surface winds at 12 and 24 h for case 9. The linear simulations (Fig. 10) are in qualitative agreement with the corresponding nonlinear simulations (Fig. 3) in the locations relative to the heat source of the minimum surface pressure, regions of ascending and descending motions, regions of maximum surface wind speed, and the surface confluence zones. For example, the maximum surface wind speed zones at 12 h in both cases 9 and 10 occur to the west and downstream of the heat source. However, the maximum wind speed at 12 h for case 9 is 11.8 m s^{-1}, compared to 9.6 m s^{-1} for case 4. Because of the stronger surface wind response in the linear case, a closed circulation can be identified in Figs. 10e

and 10f, but not in the corresponding nonlinear case (Figs. 3e and 3f). The stronger wind speed in case 9 corresponds to a deeper surface pressure minimum (-30 and -50 Pa at 12 and 24 h, respectively; Figs. 10a and 10b) than that in case 4 (-27 and -33 Pa at 12 and 24 h, respectively; Figs. 3a and 3b). The vertical velocity response for the linear case is similar to the nonlinear response. In both cases 4 and 9, the maximum ascending motion at 12 h is roughly 0.07 m s^{-1} over the heat source.

Quantitative differences are also found between the nonlinear (case 5, Figs. 4a–f) and linear (case 10, Figs. 11a–f) simulations under easterly basic wind. In this case, the nonlinear responses of surface pressure and near-surface vertical velocity are stronger than their counterparts in the linear simulation. However, the perturbation surface wind speed is larger in the linear case (Figs. 11a and 11b) than in the corresponding nonlinear case (Figs. 4a and 4b).

The differences in surface responses between northerly and easterly basic wind cases indicates that the effects of nonlinearity are influenced by the direction of the basic wind. This may be explained by the dependence of flow responses to the Froude and Rossby numbers of the total flow. Take the northerly basic wind case for example. For a steady heat source of uniform depth, these two numbers depend on the ambient wind speed. As the wind speed increases, both Froude number and Rossby number increase, and the effect of diabatic heating decreases. Therefore, for a steady heat source, there is a negative feedback between the total wind speed and the effect of diabatic heating. In areas where the perturbation wind opposes the basic flow, the total wind speed is smaller, which leads to a stronger nonlinear effect, while in areas where the perturbation wind is aligned with the basic wind, the total wind speed is large, which leads to a reduced nonlinear effect. For example, Figs. 12a–d show the sum of the nonlinear terms in the governing equations at 12 h for u, v, w, and θ, respectively. The large negative advection of u ($-\mathbf{V} \cdot \nabla u$, Fig. 12a) and positive advection of v ($-\mathbf{V} \cdot \nabla v$, Fig. 12b) in the vicinity of the heat source cause the flow to deflect westward there (Fig. 3e). Additionally, the large positive advection of v between $y = -75$ km and $y = 25$ km near $x = 30$ km and the negative advection of v between $y = -250$ km and $y = 0$ km and $|x| = 25$ km (Fig. 12b) may cause the maximum wind speed region near $y = -100$ km and $x = -25$ km (Fig. 3e) to propagate downstream. Similarly, the negative advection of θ ($-\mathbf{V} \cdot \nabla\theta$) near the center of the heat source (Fig. 12d) contributes to the decrease of temperature, which consequently leads to a higher pressure in the vicinity of the heat source. However, the vertical velocity in the linear simulation (Fig. 10c) is similar to that of the corresponding nonlinear simulation (Fig. 3c), although the advection is negative in the vicinity of the heat source (Fig. 12c). This suggests that the effect of nonlinear processes is more complicated than just the ad-
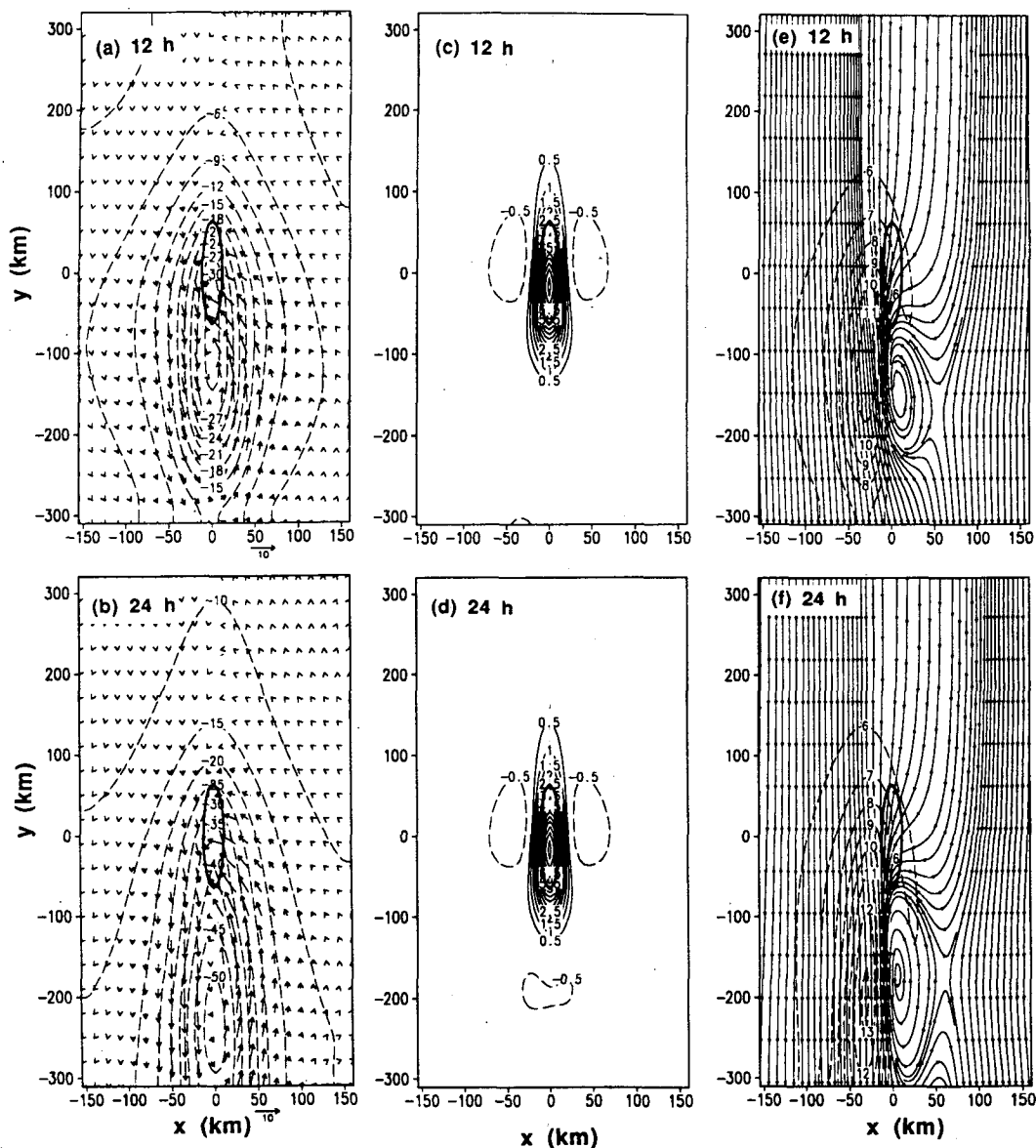
FIG. 10. Same as in Fig. 3 except for case 9.

vection terms in each equation. The interaction between the nonlinear and linear terms can be significant. For example, the temperature change caused by temperature advection may modify the pressure gradient force, which, in turn, may affect the momentum, although the pressure gradient force appears as a linear term in the momentum equations. In real situations, stronger winds may also enhance the surface heat flux (which is represented by the prescribed heating here), thus compensating the nonlinear effect discussed above. An analysis of the coupling between the heat source and the induced flow will be pursued in a separate study.

Next, consider the differences in vertical structure of the flow responses between the linear and nonlinear

cases. This can be done by comparing the differences in the respective vertical cross sections parallel to the basic wind through the center of the heat source in both linear and nonlinear cases. The vertical velocities at 24 h simulated in the northerly and easterly basic wind cases are shown in Figs. 13a and 13b, respectively. Under northerly basic wind, the linear simulation (case 9) shows that ascending motion is confined below 2 km and remains in the vicinity of the heat source (Fig. 13a), similar to the corresponding nonlinear simulation (case 4, Fig. 6a). However, in the corresponding nonlinear case, weak ascending motion develops downstream of the heat source. This suggests that nonlinearity may enhance the vertical velocity downstream of the heat source. In the easterly basic wind cases, both
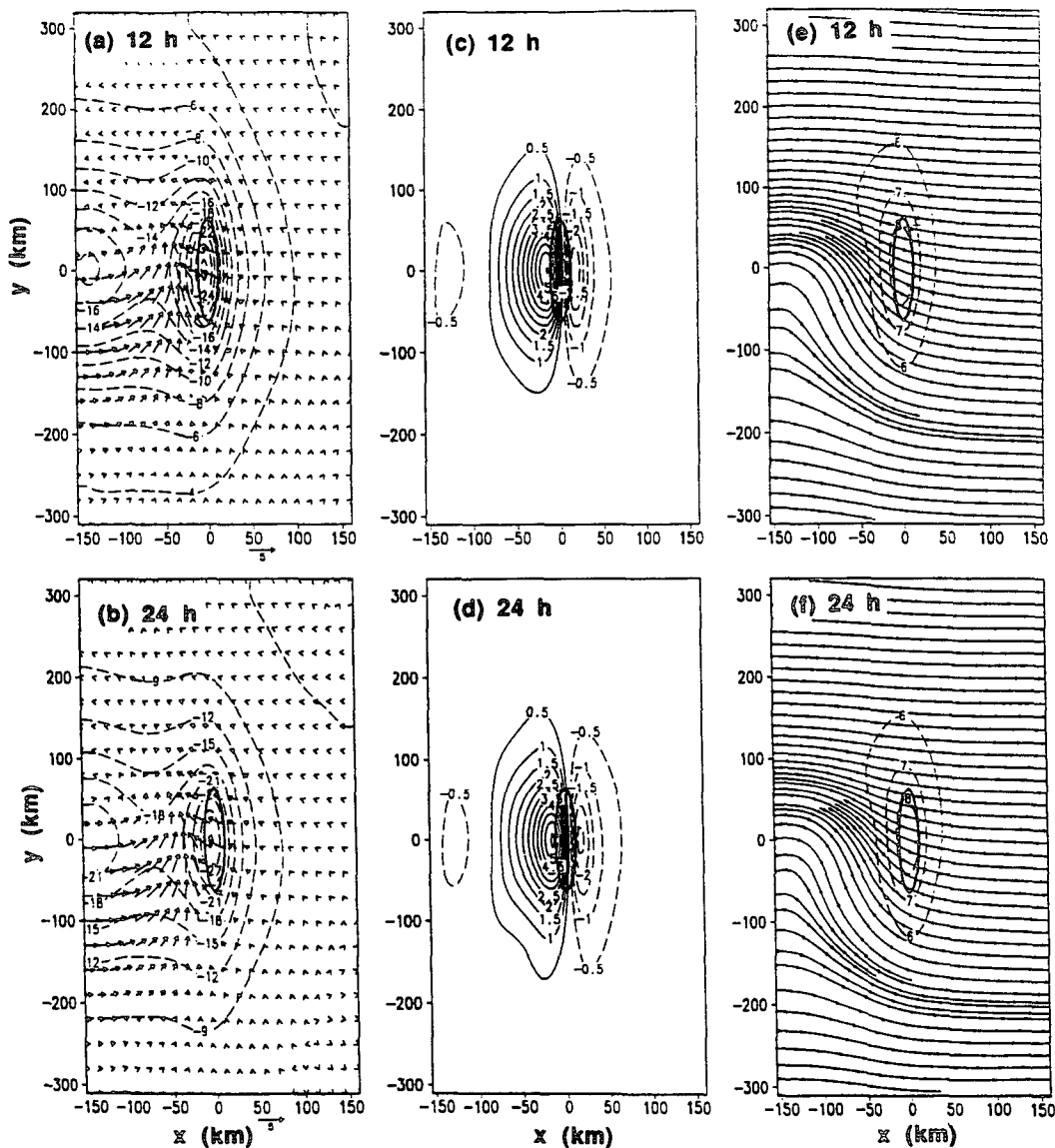
FIG. 11. Same as in Fig. 4 except for case 10.

linear (case 10, Fig. 13b) and nonlinear simulations (case 5, Fig. 6b) show that the response is characterized by upward propagating inertia–gravity waves. It is evident that the heat-induced vertical velocity in the nonlinear simulation is stronger than that in the corresponding linear simulation for easterly basic wind.

6. Application to Carolina coastal frontogenesis

The above results indicate that low-level flow responses to 3D mesoscale near-surface axisymmetric and that elongated heat sources are fundamentally different, and, in the latter case, the response is sensitive to the basic wind direction. North–south-elongated, elliptical heat sources considered in this study are representative of the diabatic heating associated with Gulf

Stream frontal features, as suggested by theoretical studies (Riordan and Lin 1992) and real data simulations (Huang and Raman 1992; Doyle and Warner 1993). Thus, existing theories on mesoscale heating by axisymmetric heat sources must be modified to take consideration of the elongated-shape effect. The horizontal aspect ratio of the alongstream scale to the cross-stream scale of the heat source determines how elongated the heat source is in the direction of the basic wind. When such a ratio is smaller than one, the response resembles that of flow over a two-dimensional heat source, and vertically propagating inertia–gravity waves are induced. However, when this ratio is large, flow can go around the heat source, and the response is more confined near the surface. The elongation of the heat source also results in a sensitivity of the re-
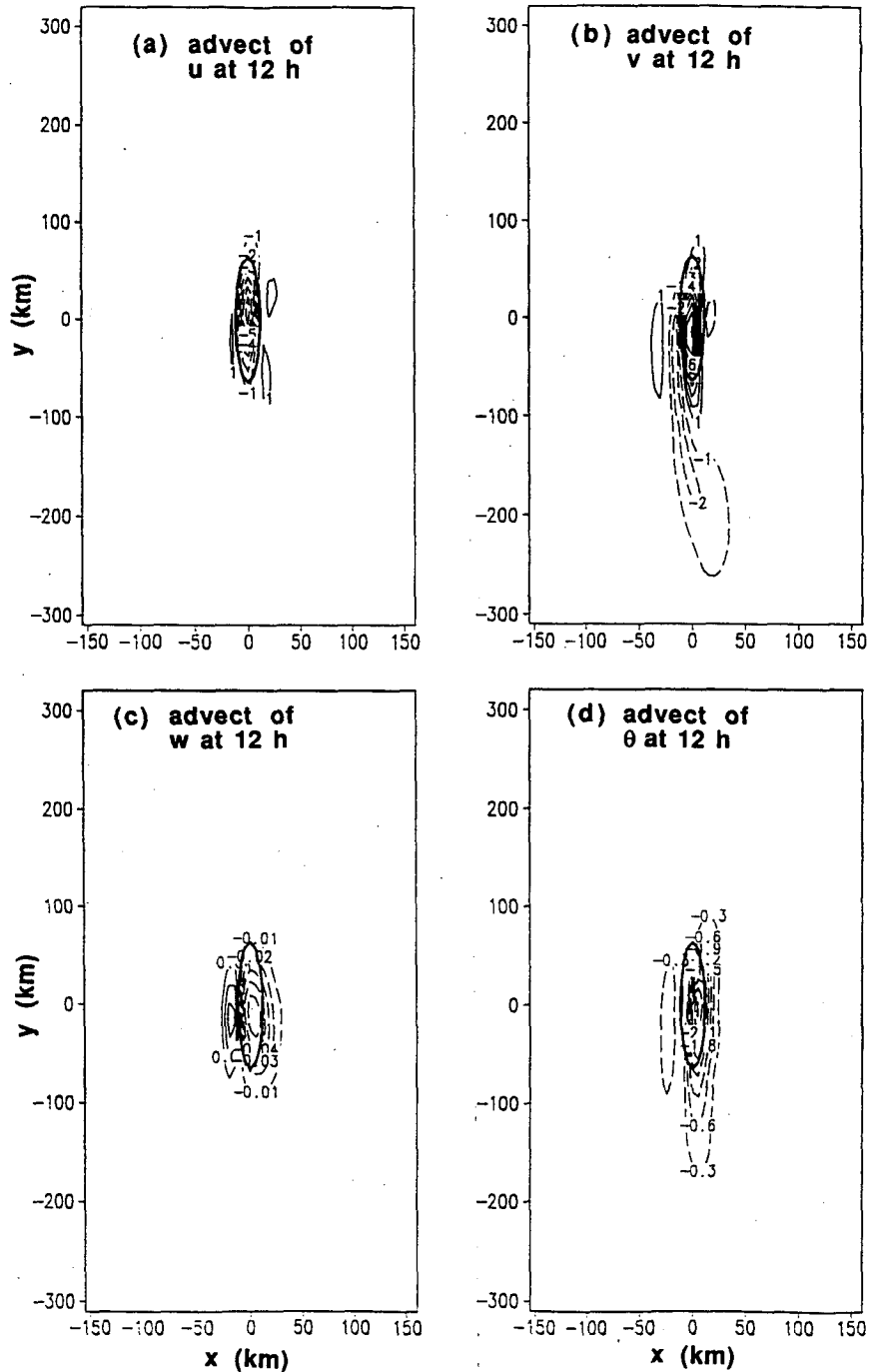
FIG. 12. Nonlinear advection under northerly basic wind at 12 h. (a) Advection of u at the surface; (b) same as (a) but for v; (c) advection of w at $z = 500$ m; (d) same as (a) but for T.

sponse of the horizontal flow pattern to basic wind direction. In the Carolina coastal environment, the coastline is generally oriented north-northeast to south-southwest. In general, the Gulf Stream front located offshore takes a similar orientation (Pietrafesa 1989), and so does the air–sea heat flux pattern (Blanton et al. 1989; Riordan 1990). A conceptual model of the

location of coastal fronts and low-level jets under various basic wind conditions can be produced based on the results from cases 4–8 with an appropriate (~45°) rotation of the coordinates and basic wind directions so that the left boundary of our model domain is roughly parallel to the Carolina coast (Fig. 14). The confluence zone and, by inference, the coast front would be located
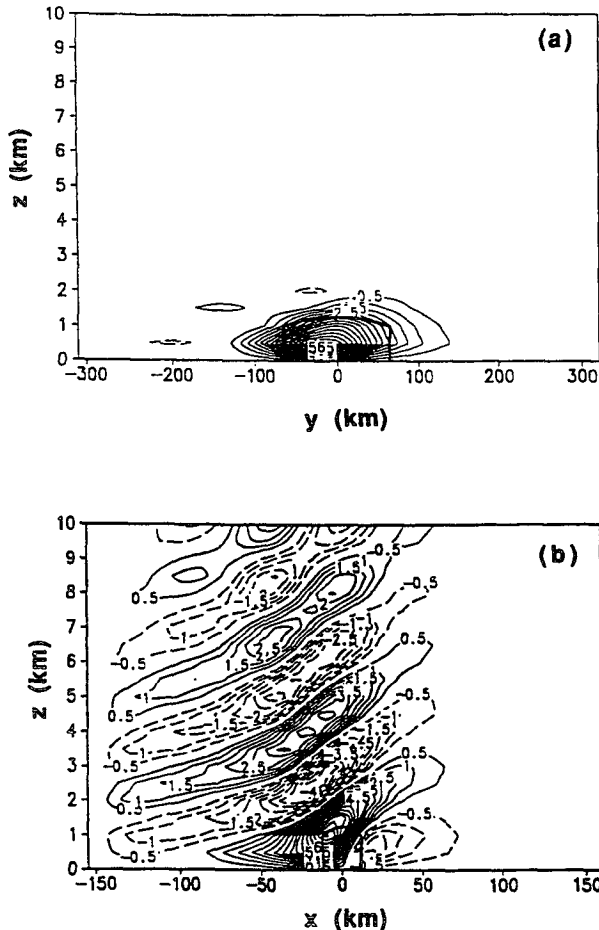
FIG. 13. Same as in Fig. 6 except for vertical cross sections of linear responses (cases 9 and 10).

along the western edge and downstream of the Gulf Stream front (in our case the major axis of the heat source) under northeasterly basic winds (i.e., parallel to the major axis of the heat source; Fig. 14a), to the southeast (seaward) of the Gulf Stream front under northerly or northwesterly basic winds (Fig. 14b), and to the west (shoreward) of the Gulf Stream front under easterly basic winds (Fig. 14c). A low-level jet would form just west of the confluence zone under northeasterly (in our case northerly) basic wind (Fig. 14a), and in the vicinity of the heat source under northerly (Fig. 14b) and easterly (Fig. 14c) basic winds (basic winds normal or with a large angle to the major axis of the heat source). Coastal fronts over the Carolina coastal waters often occur under northerly wind conditions. Based on the conceptual model, frontogenesis is predicted to occur to the southeast of the major axis of the heat source. This is supported by mesoscale analysis of the observations obtained during GALE IOP 2 (Riordan 1990).

We have also shown that an elongated heat source can effectively accelerate the low-level winds. Under a

northeasterly (northerly in our case) basic wind condition, large wind speeds appear to the west and downstream of the heat source. This may induce a divergent ocean surface current in the region of surface heating, and consequently a weakening of the SST front, and thus reduces the sea-to-air heat fluxes. Therefore, there is a negative air–sea feedback in this case. Under easterly basic wind conditions, large winds are located over, and just upstream of, the heat source. The wind-induced cross-shelf surface current would advect the warm upper Gulf Stream water westward and enhance the cross-shelf SST gradient, which would further enhance the surface wind speed. Strong coupling between the surface wind field and the heat source may exist in this case (Xie et al. 1994).

7. Conclusions

We have presented simple numerical model results of the nonlinear responses of a stratified flow to circular heat sources under northerly basic winds, and to elongated heat sources under uniform northerly, northeasterly, northwesterly, and easterly basic winds, and linear responses under northerly and easterly basic winds. It appears that the responses of a stratified airflow to 3D mesoscale heating depend not only on the Froude and Rossby numbers associated with the heat source, but also on the alongstream to cross-stream aspect ratio of the heat source. Specifically, the following can be seen.

1) In all cases with a large Rossby number ($Ro > 1$) and small Froude number ($Fr = 0.5$) associated with the respective thermal forcing, the surface pressure perturbation shows two modes: one over the heat source and another downstream (cases 1, 3, 5, 7, 8, and 10), while only one pressure minimum appears in cases with either a large Froude number ($Fr > 1$) or a small Rossby number ($Ro < 0.5$) (cases 2, 4, 6, and 9).

2) For axisymmetric heating, the response pattern is sensitive to the Froude number associated with the heating. For relatively small Froude number ($Fr = 0.5$), a stratified airstream descends and accelerates as it approaches the heat source (cases 1 and 3). The airstream then ascends over the heating region. At large Froude number ($Fr = 1.5$), ascending motion occurs downstream of the heat source with weak descending motion occurring on each side of the ascending motion. For an elongated heat source, the phase relationship between the heating and the induced perturbation also depends on the aspect ratio of the alongstream to the cross-stream scale of the heat source. We have demonstrated that, for $Fr = 0.5$, ascending motion occurs over the heat source and that no significant descending motion can be found when the aspect ratio is significantly greater than one (case 4). However, significant descending motion occurs over the upstream portion of the heat source and ascending motion occurs over the downstream portion of the heat source when this aspect ratio is less than one (case 5). At large Froude number
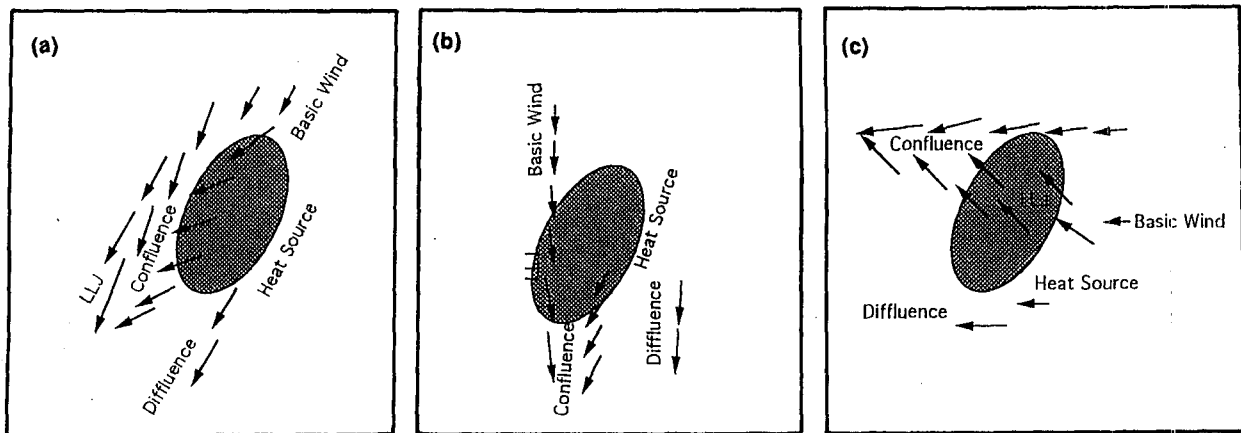
FIG. 14. A conceptual model for the formation of confluence zones and low-level jets under various basic wind conditions. Panels (a), (b), and (c) are for northeasterly, northerly, and easterly basic wind conditions, respectively.

(Fr = 1.5), descending motion occurs over the heat source and ascending motion occurs downstream (case 6).

3) The ratio of the alongstream and cross-stream scales of the heat source (determined by the shape of the heat source and the basic wind direction) has a significant impact on the vertical structure of the induced vertical motion. When the basic flow is aligned with the major axis of the heat source, the resulting vertical motion is weak and confined in the lower atmosphere, since air parcels are able to go around the heat source (cases 4 and 9). However, vertically propagating inertia–gravity waves are generated when the basic flow is perpendicular to the major axis of the heat source (cases 5, 6, and 10).

4) Airflow responses to elongated heating differ significantly from that produced by axisymmetric heating. For a north–south-elongated heat source, surface winds intensify upstream and over the heat source under easterly basic winds. Under northerly basic winds, acceleration occurs downstream and to the west of the heat source. From an air–sea interaction point of view, 3D diabatically induced mesoscale circulations under uniform easterly basic winds would enhance the shoreward advection of coastal water along the East Coast. In the Carolina coastal region, the coastline is generally northeast–southwest oriented, and a proper adjustment of the wind direction must be taken into account before applying our finding to this region.

5) Although both axisymmetric and elongated heat sources induce an SCZ over or downstream of the prescribed heating, the geometry and location of the SCZ differ considerably in each case. For an elongated heat source, the SCZ occurs along the right edge of the heat source (facing downstream) and extends far downstream when the basic wind is parallel to the major axis of the heat source. When the basic wind blows at a large angle relative to the major axis of the heat source, the confluence zone occurs downstream and is located a short distance from the heat source.

6) Linear responses are in qualitative agreement with the corresponding nonlinear responses for the particular uniform basic wind and heating fields considered in this study. However, significant quantitative difference exists between linear and nonlinear responses. These differences seem to be sensitive to the basic wind direction.

To conclude, we stress that although the present study provides some physical insight to the problem of coastal frontogenesis induced by diabatic heating, the results presented above are based on the simulated response to prescribed low-level heating. These results are qualitatively consistent with observations. However, due to the simplicity of the model, several limitations of this study should be noted. First, the model is hydrostatic. Even though the flow considered in our study falls within the hydrostatic regime, cautions should be made when applying our results to real coastal frontogenesis cases, particularly when convective-scale features are the subjects of comparison. Secondly, the diabatic heating field is prescribed in the model. Thus, there is no feedback from the kinematic field to the heating field. This approximation may lead to an unrealistic temperature field that is strongly influenced by diabatic heating. In fact, although the model produced a significant horizontal temperature gradient in the surface confluence zone, the largest near-surface horizontal temperature gradient occurred in the area of the largest heating gradient. This can be improved by implimenting a more realistic boundary layer parameterization in the model in a future study. Furthermore, coastal frontogenesis often occurs in regions where significant low-level baroclinicity exists in the large-scale environment. However, in this study, we have assumed a horizontally uniform basic temperature field and a

vertically uniform basic wind field. Thus, the results of this study may not be able to compare with observed coastal frontogenesis directly. Therefore, to build a general purpose conceptual model for the formation of Carolina coastal fronts, low-level jets, and mesoscale vortices, a more realistic mesoscale model is required. Using such a model, sensitivities of Carolina coastal frontogenesis to basic wind directions, shape of Gulf Stream frontal features, and nonlinear interactions between mass and momentum fields can be examined to validate our results under more general conditions. Before thorough verifications are made, caution should be taken when interpreting the results presented here to general real data cases.

REFERENCES

Austin, P. M., 1941: Favorable conditions for cyclogenesis near the Atlantic coast. *Bull. Amer. Meteor. Soc.,* **22,** 270–272.

Ballentine, R. J., 1980: A numerical investigation of New England coastal frontogenesis. *Mon. Wea. Rev.,* **108,** 1479–1497.

Blanton, J. O., J. A. Amft, D. K. Lee, and A. J. Riordan, 1989: Wind stress and heat fluxes observed during winter and spring 1986. *J. Geophys. Res. (Oceans),* **94,** 10 686–10 698.

Bosart, L. F., 1975: New England coastal frontogenesis. *Quart. J. Roy. Meteor. Soc.,* **101,** 957–978.

——, and S. C. Lin, 1984: A diagnostic analysis of the Presidents' Day storm of February 1979. *Mon. Wea. Rev.,* **112,** 2148–2177.

Bretherton, C., 1988: Group velocity and the linear response of stratified fluids to internal heat or mass sources. *J. Atmos. Sci.,* **45,** 81–93.

Carson, R. B., 1950: The Gulf Stream fronts: A cause of stratus on the lower Atlantic coast. *Mon. Wea. Rev.,* **78,** 91–101.

Doyle, J. D., and T. T. Warner, 1993: Nonhydrostatic simulations of coastal mesoscale vortices and frontogenesis. *Mon. Wea. Rev.,* **121,** 3371–3392.

Garstang, M., P. D. Tyson, and G. D. Emmitt, 1975: The structure of heat island. *Rev. Geophys. Space Phys.,* **13,** 139–165.

Hsu, H.-M., 1987: Mesoscale lake-effect snowstorms in the vicinity of Lake Michigan: Linear theory and numerical simulations. *J. Atmos. Sci.,* **44,** 1019–1040.

Huang, C.-Y., and S. Raman, 1992: A three-dimensional numerical investigation of a Carolina coastal front and Gulf Stream rainband. *J. Atmos. Sci.,* **49,** 560–584.

Klemp, J. B., and D. Durran, 1983: An upper boundary condition permitting internal gravity wave radiation in numerical mesoscale models. *Mon. Wea. Rev.,* **111,** 430–444.

Lin, Y.-L., 1994a: Airflow over mesoscale heat source. Part I: Responses in a uniform flow. *NSC,* **18,** 1–32.

——, 1994b: Airflow over mesoscale heat source. Part II: Responses in a shear flow. *NSC,* **18,** 119–150.

——, and R. B. Smith, 1986: Transient dynamics of airflow near a local heat source. *J. Atmos. Sci.,* **43,** 40–49.

——, and R. E. Stewart, 1991: Diabatically forced meso-scale circulations. *Advances in Geophysics,* Vol. 33, Academic Press, 267–305.

——, and T.-A. Wang, 1996: Flow regimes and transient dynamics of two-dimensional stratified flow over an isolated mountain range. *J. Atmos. Sci.,* **53,** 139–158.

Mahrer, Y., and R. A. Pielke, 1976: Numerical simulation of the airflow over Barbados. *Mon. Wea. Rev.,* **104,** 1392–1402.

Malkus, J. S., and M. E. Stern, 1953: The flow of a stable atmosphere over a heat island, Part I. *J. Meteor.,* **10,** 30–41.

Nielson, J. W., 1989: The formation of New England coastal fronts. *Mon. Wea. Rev.,* **117,** 1380–1401.

Olfe, D. B., and R. L. Lee, 1971: Linearized calculation of urban heat island convection effects. *J. Atmos. Sci.,* **28,** 1374–1388.

Pielke, R. A., 1984: *Mesoscale Meteorological Modeling.* Academic Press, 612 pp.

Pietrafesa, L. J., 1989: The Gulf Stream and wind events on the Carolina capes shelf. NOAA-NURP (National Undersea Research Program) Research Rep. 19-2, 89–129.

Raymond, D. J., 1986: Prescribed heating of a stratified atmosphere as a model for moist convection. *J. Atmos. Sci.,* **43,** 1101–1111.

Riordan, A. J., 1990: Examination of the mesoscale features of the GALE coastal front of 24–25 January 1986. *Mon. Wea. Rev.,* **118,** 258–282.

——, and Y.-L. Lin, 1992: Mesoscale signatures along the Carolina coast. *Mon. Wea. Rev.,* **120,** 2786–2797.

Smith, R. B., 1979: The influence of mountains on the atmosphere. *Advances in Geophysics,* Vol. 21, Academic Press, 87–230.

——, and Y.-L. Lin, 1982: The addition of heat to a stratified airstream with application to the dynamics of orographic rain. *Quart. J. Roy. Meteor. Soc.,* **108,** 353–378.

Uccellini, L. W., R. A. Petersen, K. F. Brill, P. J. Kocin, and J. J. Tuccillo, 1987: Synergistic interactions between an upper-level jet streak and diabatic processes that influence the development of a low-level jet and a secondary coastal cyclone. *Mon. Wea. Rev.,* **115,** 2227–2261.

Weglarz, R. P., 1994: Three-dimensional geostrophic adjustment of homogeneous and continuously stratified flows with application to the dynamics of mid-latitude jet streaks. Ph.D. dissertation, North Carolina State University, 414 pp.

——, and Y.-L. Lin, 1994: Geostrophic adjustment and jetogenesis due to impulsive and propagating zonal momentum sources in a rotating atmosphere. Preprints, *Sixth Conf. on Mesoscale Processes,* Portland, OR, Amer. Meteor. Soc., 324–327.

Xie, L., and Y.-L. Lin, 1994: Asymmetry of surface wind field forced by an elongated surface heat source. Preprints, *Sixth Conf. on Mesoscale Processes,* Portland, OR, Amer. Meteor. Soc., 274–277.

——, L. J. Pietrafesa, and S. Raman, 1994: Interaction between low-level jet and surface heat source in the Carolina capes. Preprints, *Second Int. Conf. on Air–Sea Interaction and on Meteorology and Oceanography of the Coastal Zone,* Lisbon, Portugal, Amer. Meteor. Soc., 155–156.